

Crown ether decorated silicon photonics for safeguarding against lead poisoning

Luigi Ranno^{1,†}, Yong Zen Tan^{2,†}, Chi Siang Ong², Xin Guo³, Khong Nee Koo⁴, Xiang Li³, Wanjun Wang³, Samuel Serna¹, Chongyang Liu⁵, Rusli³, Callum G. Littlejohns⁶, Graham T. Reed⁶, Juejun Hu¹, Hong Wang³ and Jia Xu Brian Sia^{1,3,*}

¹Department of Materials Science & Engineering, Massachusetts Institute of Technology, Cambridge, M.A., USA

²Fingate Technologies, Singapore

³School of Electrical and Electronic Engineering, Nanyang Technological University, 50 Nanyang Avenue, 639798, Singapore

⁴Vulcan Photonics, Kuala Lumpur, Malaysia

⁵Temasek Laboratories, Nanyang Technological University, 50 Nanyang Avenue, 637553, Singapore

⁶Optoelectronics Research Centre, University of Southampton, Southampton SO17 1BJ, UK

[†]These authors contributed equally

**Corresponding author: jxbsia@mit.edu, jiaxubrian.sia@ntu.edu.sg*

Lead (Pb²⁺) toxification in society is one of the most concerning public health crises that remains unaddressed. The exposure to Pb²⁺ poisoning leads to a multitude of enduring health issues, even at the part-per-billion scale (ppb). Yet, public action dwarfs its impact. Pb²⁺ poisoning is estimated to account for 1 millions deaths per year globally, which is in addition to its chronic impact on children. With their ring-shaped cavities, crown ethers are uniquely capable of selectively binding to specific ions. In this work, for the first time, the synergistic integration of highly-scalable silicon photonics, with crown ether amine conjugation via Fischer esterification in an environmentally-friendly fashion is demonstrated. This realizes a photonic platform that enables the *in-situ*, highly-selective and quantitative detection of various ions. The development dispels the existing notion that Fischer esterification is restricted to organic compounds, laying the ground for subsequent amine conjugation for various crown ethers. In this work, the platform is engineered for Pb²⁺ detection, demonstrating a large dynamic detection range of 1–262000 ppb with high selectivity against a wide range of relevant ions. These results indicate the potential for the pervasive implementation of the technology to safeguard against ubiquitous lead poisoning in our society.

1. Introduction

Anthropogenic lead poisoning represents one of the primary public health concerns since antiquity¹. Pb^{2+} is a cumulative toxicant that leads to multi-faceted impact on biological functions in the long term²⁻¹¹. Pb^{2+} has the affinity to substitute other bivalent and monovalent cations. For instance, Pb^{2+} can replace Ca^{2+} ions to cross the blood-brain barrier, resulting in neurological deficits⁷. This effect is exacerbated in children due to the ongoing development of their neurological and nervous system⁸. Pb^{2+} is also found to impact cardiac function, causing reduction in the speed of heart contraction and relaxation¹⁰. Furthermore, fetal exposure can result in a wide array of risks during pregnancy⁹. The above examples only serve to highlight a non-exhaustive overview of the impact of lead on our society, and many other detailed studies are available to interested readers¹¹⁻¹⁶. However, public action against lead toxification is disproportional to its impact. It has been estimated that lead service lines still deliver drinking water to about ten million households in the US alone¹⁷. The impact of lead leads to the common conclusion that there should be zero-tolerance to lead exposure¹⁸. To that effect, the Environmental and Energy Law Program (EPA), US has implemented a limit of 15 parts-per-billion (ppb) in drinking water¹⁹. Lead poisoning is even more pronounced in developing countries, where the World Health Organization (WHO) estimates that of the 240 million people that are overexposed, 99 % comes from developing countries^{20,21}. Lead exposure accounts for more than one million deaths annually, with significant societal and economic costs, specifically in developing countries²². These facts highlight the urgency for the development of technologies that guards against lead toxification.

Contemporary methods for lead detection can be grouped into two primary categories: Inductively Coupled Plasma-Mass Spectrometry/Optical Emission Spectroscopy (ICP-MS/OES)^{23,24}, and colorimetric test strips²⁵. The former represents the state-of-art, but however,

suffers from low sample throughput, requiring lengthy and expensive sample preparation and analysis by trained personnel. Furthermore, such systems are dedicated for lab use only, and not viable for on-site, *in-situ* analysis²⁴. Colorimetric test strips, while low-cost and widely available, are qualitative and might lack accuracy in detection²⁵. The development of Pb²⁺ sensors presented in this work combines the advantages of both technologies: highly quantitative and selective sensing as well as rapid, portable detection capabilities.

The photonic sensor platform makes use of crown ethers, cyclic polyethers consisting of multiple oxygen atoms forming a ring structure^{26,27}. This class of compounds were first synthesized by Charles Pederson in the 1960s, who was subsequently awarded the 1967 Nobel prize for this discovery^{28,29}. As a result of the cavity which arises from the ring structure, crown ethers possess a remarkable ability to selectively bind to certain ions or molecules based on their properties such as size selectivity charge accommodation, ring geometry and structure energetic favorability²⁸⁻³⁰. Thus far, crown ethers have employed electrochemical³¹⁻³³ and fluorescent³⁴⁻³⁶-based detection schemes. However, scaling these technologies to low-cost large sensor arrays for widespread detection remains a major challenge.

In this manuscript, we demonstrated, for the first time, a crown ether functionalized silicon photonics platform. Traditionally, the functionalization of crown ether on silicon involves the use of silylating agents with trisubstituted silyl groups which are moisture and pH sensitive, and require stringent process control^{37,38}. In the above protocol, the reagents can potentially undergo self-reaction, resulting in agglomeration, which decreases surface uniformity and negatively impacts sensor reproducibility^{37,38}. The application of the Fischer esterification protocol³⁹ to couple carboxylic acid groups with the -OH group on pretreated SiO₂/silicon waveguides surfaces, first demonstrated in this study, can circumvent the aforementioned

problem and produce the uniform amine conjugation of crown ethers on waveguide surfaces. We note that the successful Fischer esterification on SiO₂/silicon defies the conventional view that the reaction is applicable to organics only³⁹. Toward a broader scope, the Fischer esterification of an inorganic material possessing an -OH group implies the agnostic-nature of the process, indicating far-reaching technological implications to replace silylation agents in cases where they are used to couple silica/silicon with organic compounds^{37,38}. For instance, different crown ethers⁴⁰⁻⁵⁰, selective to various ions (i.e., K⁴³, Be⁴⁴, Ra⁴⁶, Cs⁴¹), illustrated at the inset of Fig. 1c, can undergo amine conjugation following Fischer esterification on SiO₂/Si, greatly broadening the range of applications (i.e., medical⁴³, electronics manufacturing⁴⁴, nuclear^{41,46}) that the developed platform can be extended to. As a corollary of complementary metal-oxide-semiconductor (CMOS) fabrication, SiP has proven to be a disruptive integrated photonic technology that enables high-precision mass manufacturing, without compromises in yield⁵¹⁻⁵⁴. Through the synergistic integration of both technologies, the resulting platform is engineered to overcome several unaddressed issues against lead poisoning in society: 1.) The successful amine conjugation of crown ethers via Fischer esterification onto aptly designed SiP circuits will enable *in-situ*, selective, ppb-scale detection of Pb²⁺ ions, improving upon current bulky lab-based systems (ICP-MS/OES)^{23,24}. 2.) ICP-MS/OES requires a significant lead time from sample collection to results due to complex lab-based sample processing and analysis^{23,24}. The work demonstrates the capacity for rapid, *in operando* determination of Pb²⁺ concentration in analytes, on site. 3.) The high-index contrast of silicon against its cladding material (SiO₂) enables the design of compact photonic sensors that can be widely applied⁵⁵⁻⁶². 4.) Through established manufacturing technologies, SiP circuits can be mass produced, at low cost⁵¹⁻⁵⁴. Furthermore, the crown-ether functionalization process is solution-based (with reactants dissolved in green solvents such as water and ethanol), implying that wafer-scale functionalization can be achieved, indicating scalability, with minimal environmental pollution.

2. Concept

2.1. Photonic Device Design

The Pb^{2+} sensor illustrated in Fig. 1a, is fabricated on the 220 nm silicon-on-insulator platform; a micrograph image is shown in Fig. 1b. Slot waveguides are implemented in the sensing arm (H_2O cladding). As the slot width is comparable to the exponential decay length of the fundamental eigenmode, optical power perpendicular to the high-index contrast interfaces is amplified^{60–65}. Essentially, this feature of slot waveguides lends to high surface sensitivity^{60–65}. The lightwave propagates to an asymmetric adiabatic tapered splitter⁶⁶ (Fig. 2d), where a larger proportion of the optical power is directed to the sensing path. Following, a 250 μm -long strip-to-slot converter is utilized for the transition of the strip to slot optical mode⁶⁵ (Fig. 2e). With the exception of the sensing region, which is exposed to the analyte, the entire device is cladded with SiO_2 . The thickness of the SiO_2 cladding is designated to be 2 μm to prevent interaction with the analyte, where $> 99\%$ of the optical power is confined within the boundaries of the cladding. In the reference arm, slot waveguides with identical dimensions are also implemented. The reason for this is to normalize waveguide propagation losses on the sensing and reference arms, and the power ratio of the asymmetrical adiabatic tapered splitters are designed according to water absorption⁶⁷ (designed losses) in the sensing region. The lightwave from the sensing and reference arms recombines at the asymmetrical adiabatic tapered splitter, forming the MZI interferometric spectrum. Power ratio of the two splitters is designed to optimize interference fringe visibility⁶⁰ (extinction ratio). The operating protocol of the sensor is elucidated in Fig. 1c. First of all, the sensing arm is exposed to deionized (DI) wafer to obtain the reference resonant wavelength (λ_0); and subsequent wavelength shift will be considered in reference to this wavelength.

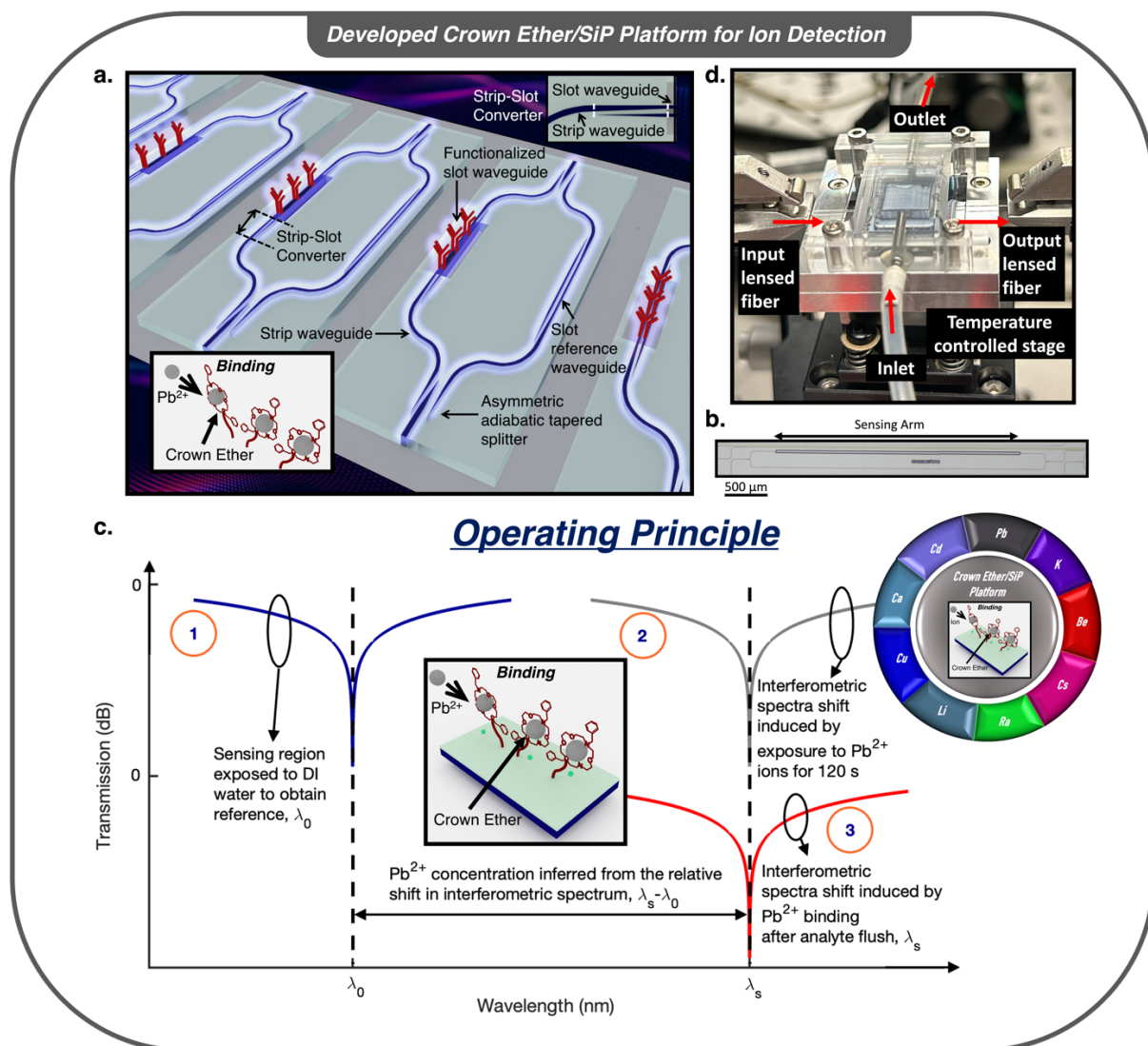


Fig. 1 Concept of the Crown Ether/SiP platform for ion detection. **a**, 3-D illustration of the photonic Pb^{2+} ion sensor based on the crown ether decorated SiP platform. The functionalization performed in the sensing arm is indicated by the features in red, where the inset illustrates the crown ether functionalized to the Si/SiO₂ surface by Fischer esterification, and then amine conjugation. **b**, The micrograph image of the Pb^{2+} ion sensor, where the sensing arm and scale bar (500 μm) are indicated. **c**, Elucidated operating principle of the photonic Pb^{2+} ion sensor. The inset shows the exemplary applications that the ion detection platform can be extended to. **d**, The Pb^{2+} photonic sensor assembly, consisting of the photonic chip and a microfluidic chamber.

Following, DI water will be flushed from the microfluidic chamber, and analyte possibly containing Pb^{2+} ions will be added. Should the analyte contain Pb^{2+} ions, a resonant shift will be induced through binding of the ions to the functionalized surface of the sensing region

through surface sensing^{56,60-62}. However, one should also note that a proportion of the wavelength shift could also be caused by the interaction of the evanescent field with the other particles/ions/molecules in the analyte⁵⁶. Therefore, this necessitates the subsequent flushing of the analyte from the device via the addition of DI water. This results in the retention of Pb²⁺ ions, which are binded to the surface of the sensor through the functionalized layer. Subsequently, the resonant shift (λ_s) measured can be attributed to the immobilized Pb²⁺ ions. The concentration of the Pb²⁺ ions in the analyte can be deduced from the shift in resonance wavelength from reference ($\lambda_s - \lambda_0$), utilizing a calibration curve; the calibration curve indicates wavelength shift as a function of detected concentration as shown later in Fig. 5b. We will henceforth refer to the flushing of analyte and the addition of DI water into the microfluidic chamber after ion interaction as analyte flush.

Fig. 1d shows the photonic chip, with the polydimethylsiloxane (PDMS) microfluidic channel mounted via a stainless-steel fixture. Analyte input and extraction was implemented via the following inlet and outlet tubes. Optical input/output was performed via edge coupling between a lensed fiber with $\sim 3 \mu\text{m}$ mode field diameter and a silicon coupler that tapers down to 175 nm. The abovementioned assembly (see Supplementary Note 1) was mounted on top of a thermoelectric controller (TEC), maintained at 296 K with thermal drift of lower than 2 mK.

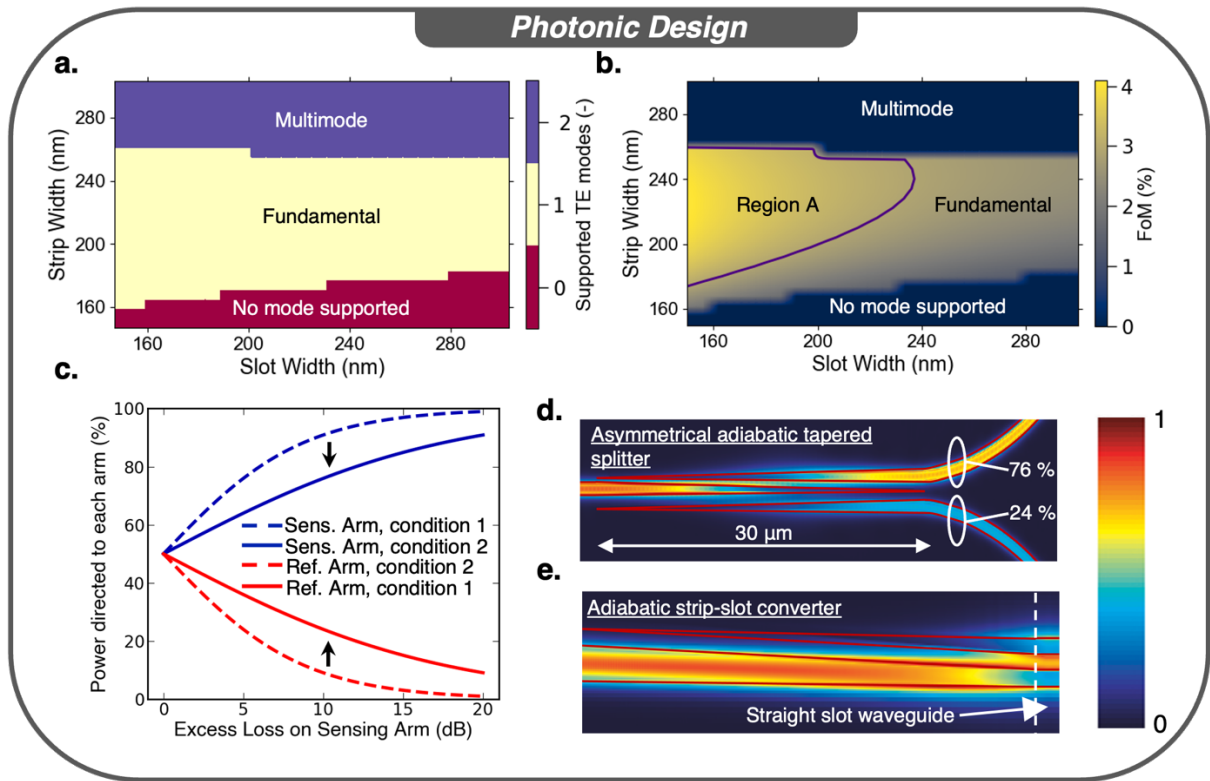


Fig. 2 Photonic design of the lead ion sensor **a**, Simulation of the number of supported TE optical modes in the slot waveguides as a function of strip and slot width. **b**, Sensor surface sensing FoM as a function of strip and slot width. **c**, The comparison of two proposed splitting Mach-Zehnder architectures (see Supplementary Note 3) in terms of the power asymmetry required of the splitter; condition 1 ($S_1 = S_2, S'_1 = S'_2, S'_{1/2} \neq 0.5$), condition 2 ($S'_1 \neq 0.5, S'_2 = 0.5$). Top-down electric field distribution of the **d**, asymmetrical adiabatic tapered splitter, and **e**, adiabatic strip-slot converter, where the structure of the components are outlined.

The dimensions of the slot waveguide (Strip and Slot width defined at Supplementary Note 2) were determined via eigenmode calculations in Fig. 2a-b, where H₂O cladding surrounds the structure. First of all, the parameter space corresponding to the number of transverse electric (TE) modes was performed in Fig. 2a. As the top and bottom media surrounding the waveguide is asymmetrical (BOX on the bottom and H₂O as the cladding), there exists a regime where the fundamental mode is not supported (in red); when the mode angle is smaller than the critical angles. Conversely, the multi-mode regime of the slot waveguide structure is indicated in blue, where the second order TE mode will be supported. According to Fig. 2a from left to right, the

second order TE mode emerges when the strip and slot widths are ~ 260 and ~ 145 nm respectively. In addition, the corresponding strip width that excites the second order TE mode decreases as slot width increases. The parameter space corresponding to single TE mode propagation is highlighted in yellow. For optimization of surface sensitivity, the selection of the optimal strip and slot width, subject to the fundamental TE mode is dependent on the optical mode confinement on the surface of the sensing region. To that effect, a figure-of-merit (FoM) is defined, that takes into consideration, the optical confinement factor within 10 nm about the surface of the slot waveguides which are cladded with 20 nm of SiO₂ (see Supplementary Note 2).

Computation of the FoM is performed in the parameter space of Fig 2(a) and the results are presented in Fig. 2b. The corresponding boundary condition for the number of supported TE modes (Fig. 2a) is replicated in Fig. 2b. As a guide to the eye, the highest value of FoM is indicated by region A. However, we have encountered difficulties in the selective removal of SiO₂ cladding at the sensing region when the slot gap is smaller than 200 nm. As such, strip and slot width of 240 and 240 nm respectively are implemented to relax process requirements; the selected slot waveguide parameters lie close to the boundary of region A.

H₂O poses significant water absorption at the C-band⁶⁷. Yet, the length of the sensing region increases the surface sensitivity of the sensor; which forces an inherent tradeoff between the fringe visibility (extinction ratio) and sensitivity^{56,60-62}. The implementation of asymmetrical splitting in MZIs will serve to overcome the issue. As identical slot waveguide dimensions are implemented on the sensing and reference arms, the primary source of loss difference between the two arms comes from water absorption. It can be concluded that the splitting ratios of the MZIs must be co-designed with the length of the sensing arm, hence designed losses. The

quantities are related to one another via the following equation, where the derivation is elaborated (see Supplementary Note 3). Designed losses through water absorption is assumed to be the only source of loss in the sensor.

$$\sqrt{S_1}\sqrt{S_2}e^{-\frac{\alpha L}{2}} = \sqrt{S'_1}\sqrt{S'_2} \quad (3)$$

S_1, S'_1 and S_2, S'_2 refers to the splitting ratios of the input and output splitter respectively. Assuming the splitters are lossless, energy conservation dictates that $S_{1/2} = 1 - S'_{1/2}$. α is the loss coefficient due to water absorption, and L refers to the length of the sensing arm. We propose a condition such that $S_1 = S_2, S'_1 = S'_2$ and $S'_{1/2} \neq 0.5$ (condition 1). In Fig. 2c, we plot the splitting ratios to the sensing and reference arm corresponding to maximum visibility. A comparison to an alternate condition where arbitrary splitting is at the input splitter, and 3-dB splitting is at the output splitter (condition 2, $S'_1 \neq 0.5, S'_2 = 0.5$) is also indicated in Fig. 2c; see Supplementary Note 3. In comparison, condition 1 reduces the asymmetry that is required of the splitters, alleviating fabrication requirements. As a compromise between the sensor surface sensitivity and the optical measurement setup power budget, our demonstration selected splitting ratios corresponding to sensor arm designed loss of 10 dB: $S_1 = 0.76, S_2 = 0.24$. In regard to the selected slot waveguide dimensions in a water cladding, the waveguide propagation loss due to H₂O absorption is estimated to be 35 dB/cm at $\lambda = 1.55 \mu\text{m}$. This gives rise to a sensing arm length of $\frac{\text{Designed Loss (dB)}}{\text{Propagation Loss (dB/cm)}} = \frac{10}{35} = 2857.14 \mu\text{m}$.

Asymmetrical adiabatic tapered splitter, which has been developed in our previous work⁶⁶, are implemented for arbitrary power splitting. These power splitter offers the advantage of broadband operation and low loss. In Fig. 2d, we show the top-down electrical field distribution of a 30 μm -long 76/24 % power splitter. The length of the strip-to-slot converter is 250 μm , where low-loss adiabatic conversion from strip to slot mode is facilitated⁶⁵. Similarly, the top-

down electric field distribution of the lightwave as it propagates along the converter is indicated in Fig. 2e.

2.2 Functionalization and Characterization of 7,16-Dibenzyl-1,4,10,13-tetraoxa-7,16-diazacyclooctadecane (DBTDA) functionalized chip via Fischer Esterification and Amine Conjugation

The functionalization protocol can be divided into four steps (Fig. 3a) with purification implemented after every step. Firstly, a layer of SiO₂ (20 nm) is deposited onto silicon via Atomic Layer Deposition (ALD) in the pretreatment step. Secondly, the Fischer esterification method³⁹ is used to couple the silanol group on the SiO₂ surface of the SiP slot waveguides (in the sensing region) with polyacrylic acid, in the presence of a tin catalyst⁶⁸; specifically tin (II) chloride dissolved in DI water. The photonic chips, immersed in the reagent, was maintained at 318 K and agitated, while the reaction proceeds for 60 minutes. The chips are then cleaned with DI water. Following, the photonic chips are functionalized with DBTA, forming amide bonds via conjugation, in the presence of 1-Ethyl-3-(3-dimethylaminopropyl)-carbodiimide), EDC, and N-Hydroxysuccinimide NHS dissolved in ethanol^{24,69}. In the final step, the functionalized photonic chips are rinsed in dilute nitric acid to remove as much of tin catalyst adsorbed on the surface as possible. This was done by placing the functionalized photonic chips in a solution of 0.1 M nitric acid, agitated with a magnetic stir bar for 60 minutes.

X-ray Photoelectron Spectroscopy (XPS) analysis was used to characterize the functionalized photonic chips before functionalization as well as, before and after interaction with different ions to analyze the resulting elemental constitution. A comparison of the N 1s region⁷⁰ of the XPS spectrums before and after functionalization (Fig. 3b) shows that the presence of nitrogen is only detected after the functionalization process. While the comparison of the C 1s region⁷⁰ of the XPS spectrums before and after functionalization (Fig. 3c) shows a larger peak area and

chemical shift of C1s carbon towards a higher binding energies (~ 286.5 eV⁷⁰, ~ 288.8 eV⁷⁰). The binding energy level at 286.5 eV indicates higher carbon concentration and significant carbon binding with electronegative species such as oxygen (C-O) and nitrogen (C-N)⁷⁰, and the peak at ~ 288.8 eV corresponds to C=O⁷⁰. Furthermore, the comparison of the O 1s region⁷⁰ of the XPS spectrums before and after functionalization (Fig. 3 d) shows a decrease in oxygen signal and chemical shift of O 1s towards a lower binding energy.

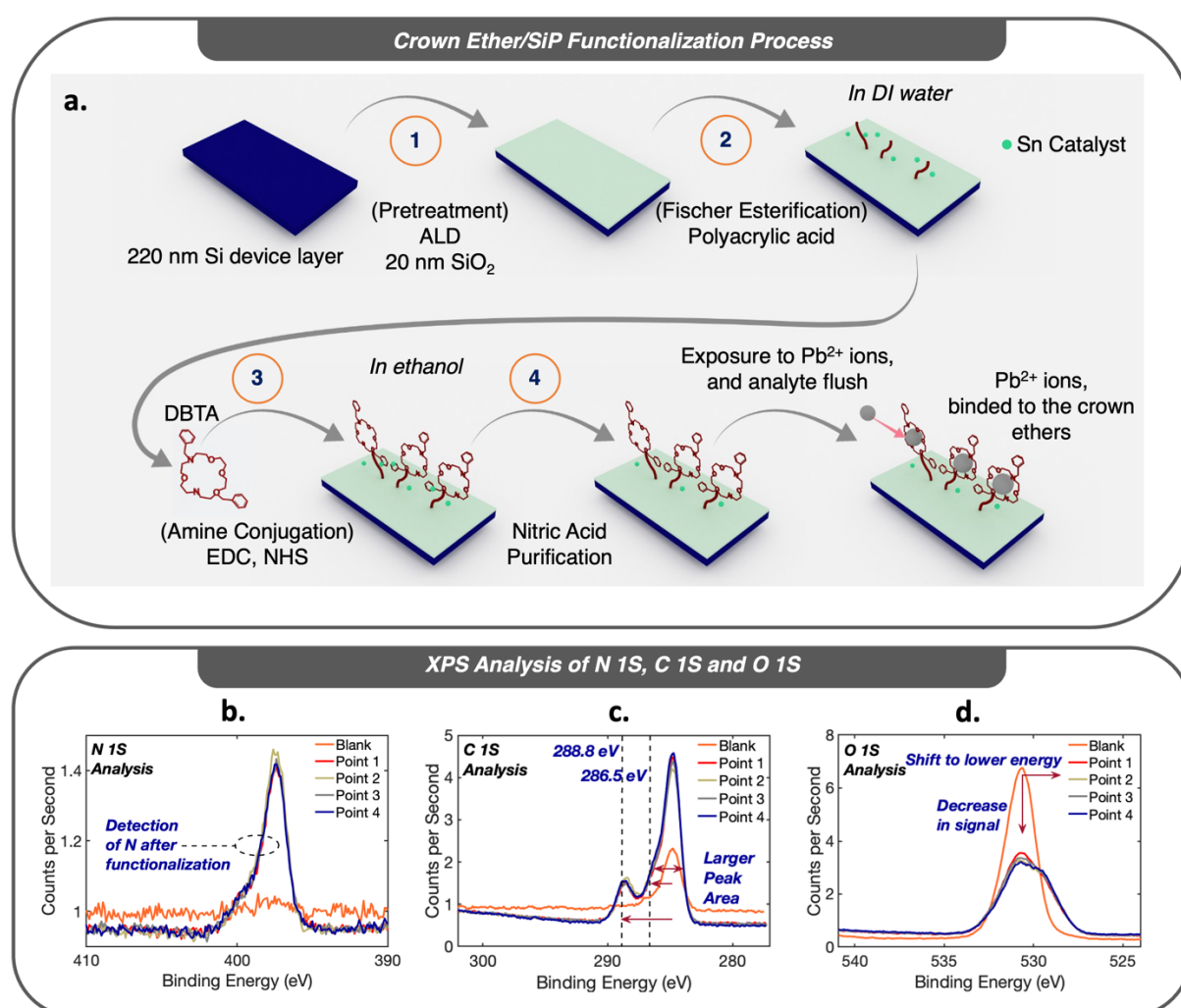


Fig. 3 The development of the Crown Ether/SiP functionalization process **a**, The developed crown ether/SiP functionalization process, described in 4 steps. XPS narrow spectra analysis of the **b**, N 1S, **c**, C 1S, **d**, O 1S regions of the photonic chips, before and after functionalization.

This observation can be attributed to the functional layer consisting of more carbon compared to oxygen⁷⁰, and the Fischer esterification of silanol with the carboxylic acid group forms O-C

bonds which have a lower binding energy compared to O-Si bonds⁷⁰. The above points to significant evidence that successful Fischer esterification have been achieved following the elucidated protocol (Fig. 3a). Furthermore, to assess the uniformity of functionalization, in Fig. 3b-d, the N 1s, C 1s and O 1s regions respectively of the XPS spectra were taken at four different points (Point 1, 2, 3, 4) on the photonic chip spaced more than 1 cm apart on the photonic chip, showing high consistency. This implies that a functional layer with good uniformity have been realized. In addition, Energy Dispersive X-ray (EDX) analysis pertaining to elemental analysis of the functional layer was performed and included in Supplementary Note 4. The results provide compelling evidence for the successful uniform functionalization of the DBTA crown ether, which contains carbon bonded to nitrogen and oxygen, via Fischer esterification and amine conjugation.

Na, K, Mg, Li, Zn, Ca, Fe, Cu, Al, Sn, Cd, and Pb were chosen as highly-relevant analytes to quantify the selectivity of the photonic-based ion detection platform. The selected ions demonstrates a variety of ionic sizes and charge. Na, K, Ca, Mg, Zn and Cu are commonly found in bottled water sources⁷¹, while Fe, Li, and Al could be present in groundwater sources⁷². Sn is used as a catalyst in the Fischer esterification process⁶⁸, and Cd and Pb⁷³ are toxic heavy metals that should be prohibited in drinking water. Each functionalized photonic chip interacts with 100 ppb of the abovementioned analyte independently for 120 s in a microfluidic chamber. After which, the analyte is flushed with DI water and dried with N₂ gas blow. XPS is utilized to identify the elemental constitution on the surface of the photonic chips before and after ion interaction via the respective elemental binding energies of each element. Normalization was carried out where the narrow scan XPS spectra prior to ion interaction was subtracted from that after ion interaction. The normalized narrow scan XPS spectra of Na, K, Mg, Li, Zn, Ca, Fe, Cu, Al, Sn, and Cd are displayed in Fig. 4a–k respectively, indicating the absence of binding

on the functionalized photonic sensor. For the abovementioned ions, we note that only Sn^{2+} , which is used as the catalyst during Fischer esterification, have been identified prior to ion interaction (see Supplementary Note 5). Conventionally, Fischer esterification is favored when H_2O is removed as the reaction proceeds (dehydrative esterification). However, the developed esterification process in this work utilizes H_2O as a green solvent, which will decrease the catalytic activity of Brønsted acid catalysts (i.e., H_2SO_4)⁷⁴. In the process (Fig. 3a), the H_2O -tolerant Lewis acid catalyst SnCl_2 , is used^{68,75} where Sn is embedded into the SiO_2 , functioning as a heterogeneous catalyst in the process. It is known that heterogeneous catalysts show improved catalytic activity⁷⁶ that favors esterification even in the presence of H_2O ⁷⁷. This is verified in Fig. 3b-d and Supplementary Fig. 4 (see Supplementary Note 4). In Fig. 4i, unmistakable binding of Pb^{2+} ions is demonstrated, indicating the presence of Pb^{2+} binding events on the functional layer, via identification of the Pb $4f_{5/2}$ and Pb $4f_{7/2}$ elemental binding energies⁷⁰. Furthermore, in Supplementary Note 4, EDX analysis is performed, where the absence and presence of Pb^{2+} can be clearly seen before and after interaction respectively. From the above, it can be anticipated that the photonic sensor will be selective only towards Pb^{2+} , where the ion will bind to the functionalized surface, and be present after analyte flushing. Subsequently, the concentration of exposed Pb^{2+} can be inferred from photonic surface sensing via the shift in the interferometric spectrum.

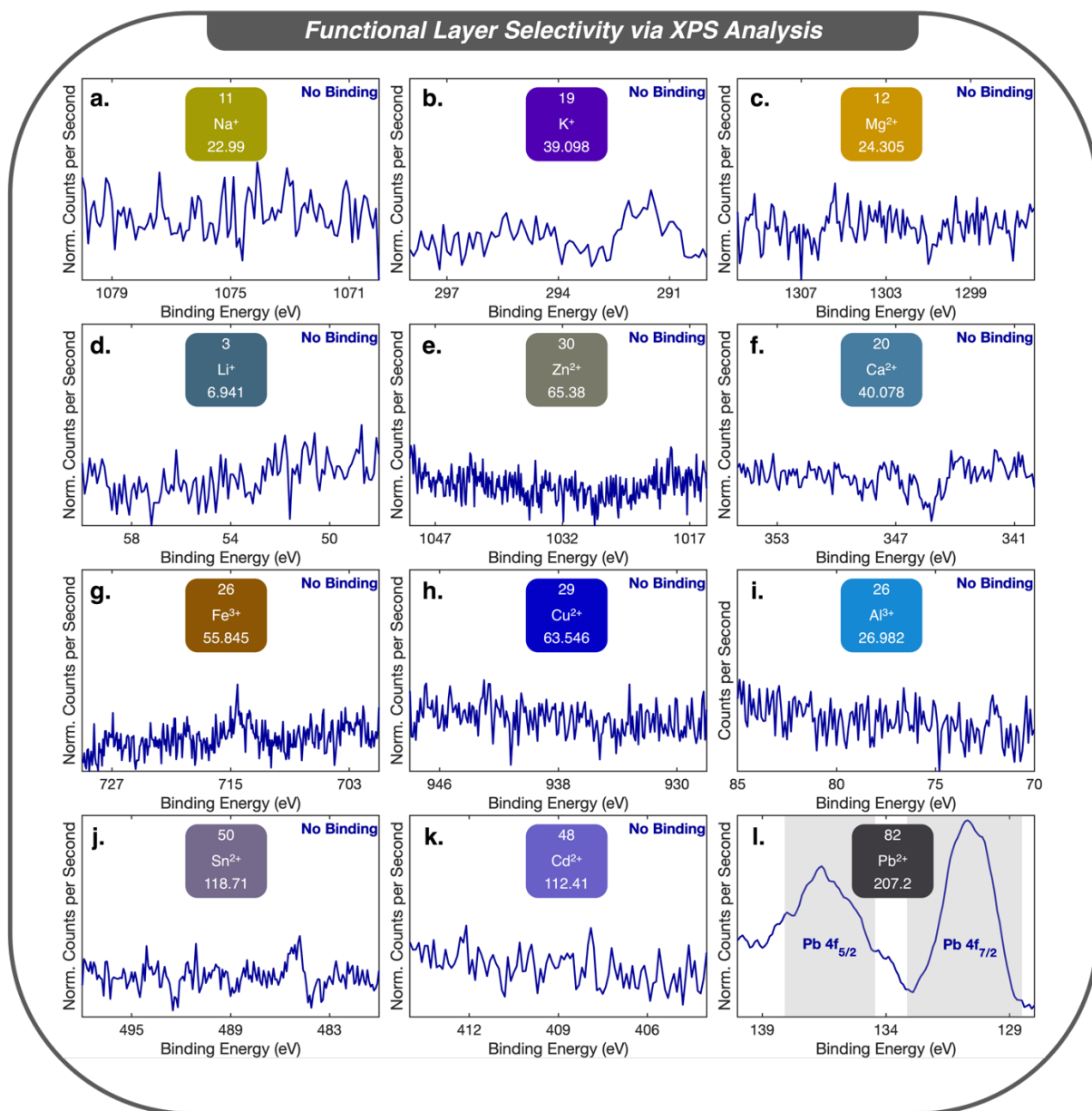


Fig. 4 Analysis of functional layer selectivity via XPS. Normalized narrow scan XPS spectra at photonic chip surface by subtracting the spectra prior to ion interaction from that of after ion interaction **a**, Na⁺, **b**, K⁺, **c**, Mg⁺, **d**, Li⁺, **e**, Zn²⁺, **f**, Ca²⁺, **g**, Fe²⁺, **h**, Cu²⁺, **i**, Al³⁺, **j**, Sn²⁺, **k**, Cd²⁺, and **l**, Pb²⁺ ions respectively.

3. Pb²⁺ Photonic Sensor Characterization

In Fig. 5a, we show the measured fundamental TE mode transmission of the functionalized photonic sensor, exposed to DI water; see Methods for maintenance of fundamental TE. Details pertaining to SiP chip fabrication is elaborated in Supplementary Note 7. As predicted, good interference fringe visibility is obtained, at $\lambda = 1531.9$ nm, where extinction ratio exceeds 20 dB. In contrast, when the sensing region is exposed to air, poor visibility is observed (see Supplementary Note 6). It is observed that sensor visibility is reduced at $\lambda = 1563.7$ nm, attributed by the lower water absorption at $\lambda = 1563.7$ nm. The experimental demonstration of the sensor visibility is limited by fabrication bias from design parameters. This would induce changes in designed splitting ratios (S_1, S'_1, S_2, S'_2), as well as loss difference between the reference and sensing arms. The measured free-spectral range (FSR) is 31.7 nm.

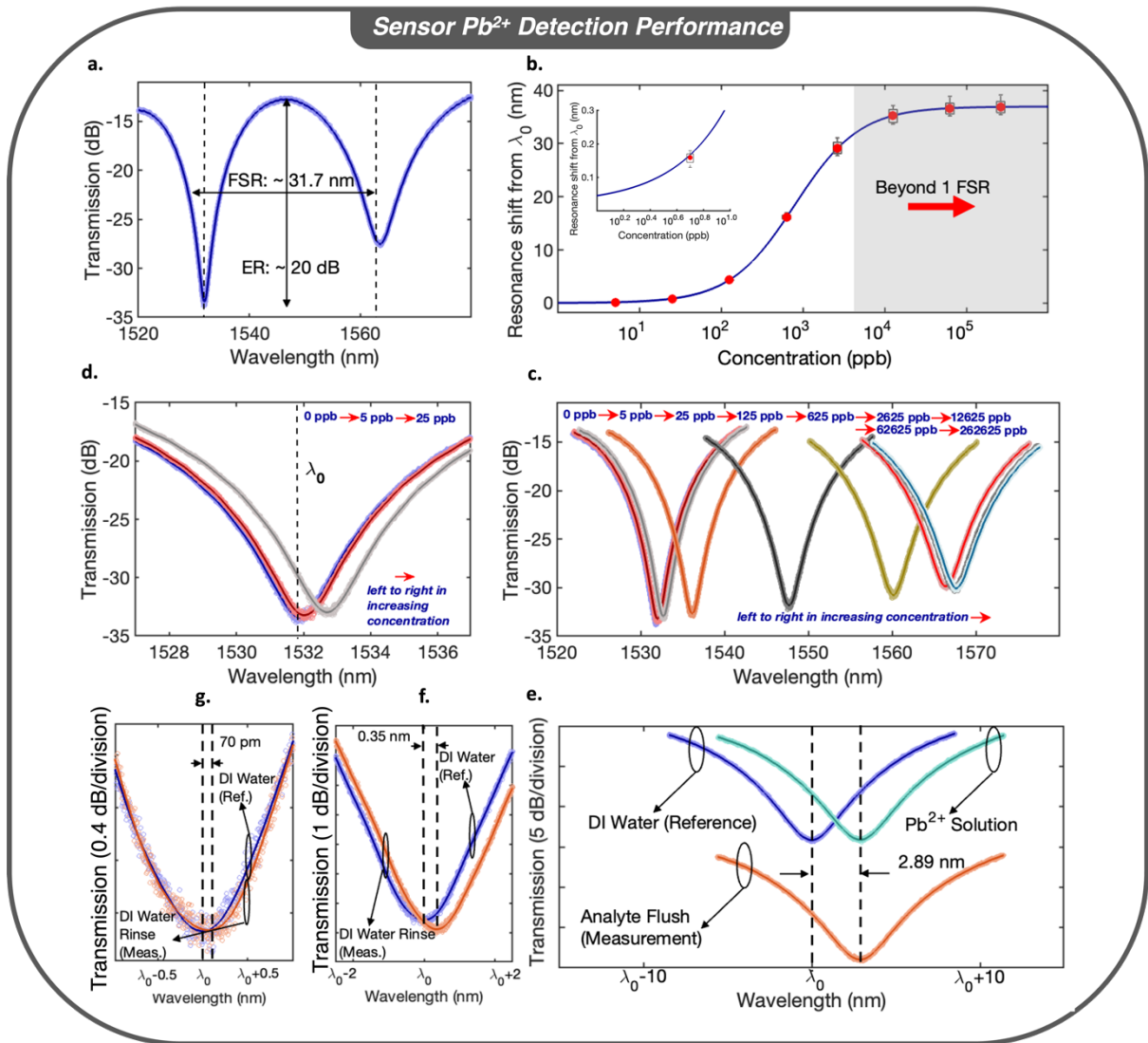


Fig. 5. Experimental characterization of Pb^{2+} sensor performance. **a**, Wavelength spectrum of the sensor, when DI water is applied into the sensor assembly (as shown in Fig. 1c). **b**, Calibration curve of the sensor when exposed to Pb^{2+} concentration of 0, 5, 25, 125, 625, 2625, 12625, 62625, 262625 ppb, via a cumulative testing approach (see Experimental Section). **c**, A set of fringe minima corresponding to the tested concentration in the calibration curve (Fig. 5b). **d**, Fig. 5c, zoomed-in at concentrations of 0, 5, 25 ppb. Validation of the calibration curve (Fig. 5b) at concentrations of **e**, 80, **f**, 10 and **g**, 1 ppb.

The calibration curve of the Pb^{2+} sensor, indicating resonant wavelength shift as a function of cumulative Pb^{2+} concentration within the analyte (5, 25, 625, 2625, 62625, 262625 ppb) is indicated in Fig. 5b through a cumulative testing process (see Methods); the inset shows the resonant wavelength shift within a range of 1 to 10 ppb. Interpolation was carried out to

understand the form of the calibration curve. The sigmoidal curve is characteristic of absorption isotherms^{78,79}. As indicated by the shaded section in Fig. 5b, the wavelength shift exceeds a single FSR when the cumulative concentration of Pb^{2+} is higher than ~ 60000 ppb. In Fig. 5c, we show a set of MZI spectra around the minima transmission points for the fringes corresponding to each of the abovementioned concentrations. As a large cumulative concentration range is presented in Fig. 5c, the spectra when cumulative Pb^{2+} concentration are 0, 5 and 25 ppb are shown (Fig. 5d). A saturation of $\lambda_s - \lambda_0$ against cumulative concentration is observed in Fig. 5b. This is ascribed to the saturation of the binding sites within the functional layer^{78,79}.

To affirm the reproducibility of the calibration curve in Fig. 5b, three photonic sensors were tested independently, at concentrations of 80, 10 and 1 ppb. In Fig. 5e, the transmission spectra when the sensing region is exposed to DI water, DI water containing 80 ppb Pb^{2+} , as well as after analyte flush of Pb^{2+} are shown. Based on the positions of λ_s in comparison to λ_0 , a $\lambda_s - \lambda_0$ of 2.89 nm is obtained. This shift was observed after analyte flushing, consistent with the binding mechanism on the surface of the sensor. By comparing this value to Fig. 5b, the inferred concentration from the calibration curve is 81.65 ppb, which is close to the actual value of 80 ppb. Similarly, Fig. 5f and 5g yield concentrations of 10.56 and 1.7 ppb as determined from the calibration curve, versus ground truths of 10 and 1 ppb respectively. The accuracy of the photonic measurement setup in determining the resonant wavelength of the sensor interferometric spectrum is ~ 20 pm, obtained from multiple spectral measurements of a sensor, at the same condition (10 ppb Pb^{2+} followed by analyte flush). This indicates that the sensor is capable of detecting Pb^{2+} at concentrations much lower than the EPA standard.

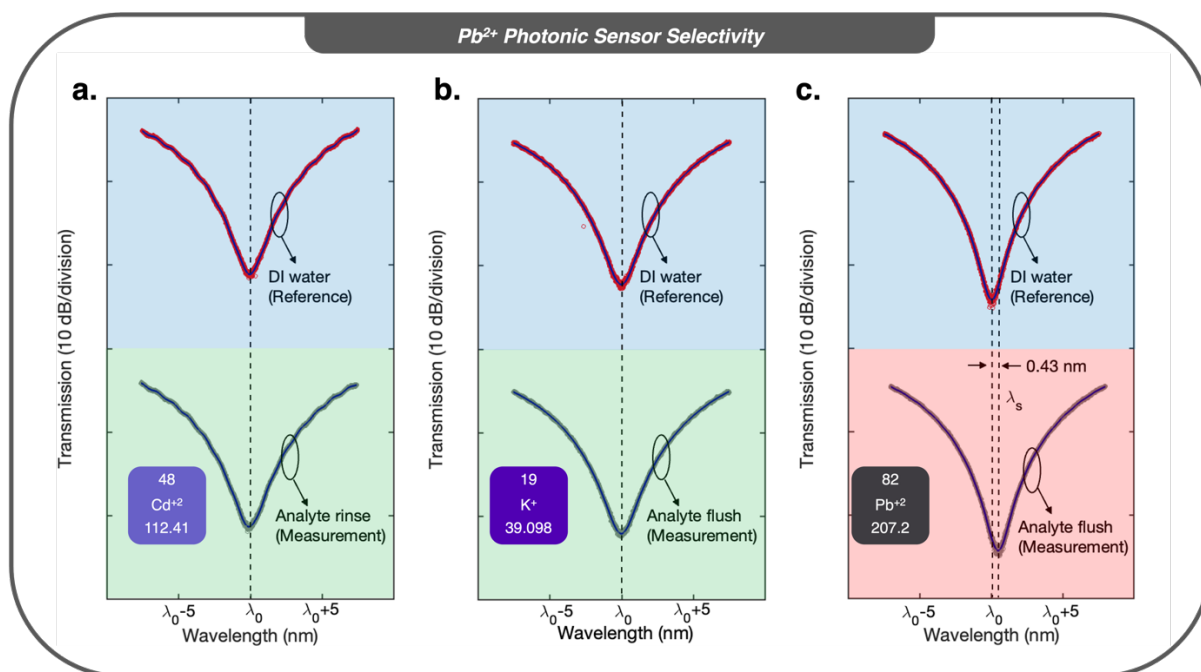


Fig. 6. Selectivity performance of the Pb^{2+} ion photonic sensor against a, Cd^{2+} , and b, K^+ at 15 ppb where no shifts in the interferometric spectra indicative of ion binding is observed. Similar to Fig. 5 e-g, the detection performance of the Pb^{2+} photonic ion sensor is tested at 15 ppb, where significant ion binding, resulting in interferometric shifts that corresponds closely to Fig. 5b is observed.

In Fig. 4 (XPS analysis), the functional layer is found to be selective to Pb^{2+} ions against the other tested ions, which implies the selectivity of the photonic sensor. To further verify sensor selectivity performance at the Pb^{2+} safety threshold (15 ppb¹⁹) Na^+ , K^+ , Mg^{2+} , Ca^{2+} , Fe^{3+} , Cu^{2+} , Sn^{2+} , Cd^{2+} are all tested at 15 ppb; Cd^{2+} and K^+ are shown in Fig. 6a-b respectively. As expected from Fig. 4, no shift in the interferometric spectrum indicative of ion binding is observed. The reference interferometric spectrum (in DI water), and the resulting spectrum after exposure and analyte flush for Cd^{2+} and K^+ are presented in Fig. 6a-b respectively and data for other ions are presented in Supplementary Note 8. The data indicates no shift in the interferometric spectrum indicative of ion binding. Similar to Fig. 5e-g, the photonic sensor was tested at 15 ppb of Pb^{2+} , where a shift of 0.43 nm corresponding to 13.1 ppb is obtained, in reference to the calibration curve in Fig. 5b. The results in Fig. 6 and Supplementary Note 8 underpins the ability of the

sensor to effectively detect Pb^{2+} ions in the presence of the other ions. A more comprehensive selectivity study is required, and is currently being conducted.

4. Conclusion

In this work, for the first time, crown ether functionalization via Fischer esterification and subsequent amine conjugation is integrated with highly-scalable, and low cost inorganic SiP. This realizes a photonic platform that enables the selective binding of Pb^{2+} ions, and subsequent detection down to the ppb-scale. The novel reaction pathway proposed and demonstrated, driven via Fischer esterification defies prior expectations that the process is restricted to organics³⁹. This enables the engineering of the platform to selectively detect a plethora of ions via subsequent amine conjugation of various crown ethers⁴⁰⁻⁵⁰. Furthermore, the functionalization process, by virtue of being solution-based, can be implemented at the wafer-scale. The reactants are dissolved in green solvents which results in minimal environmental impact. The sensor presented in this work indicates the ability to detect Pb^{2+} concentrations *in-situ*, through a wide dynamic range (1 – 262000 ppb) while being highly-selective against other commonly-found, relevant ions. This work represents an encouraging step towards the ubiquitous implementation of photonic-based sensors that protects against widespread Pb^{2+} poisoning. We envisage that this platform can be extended to multiplex ion detection in multiple application spheres.

Methods

Microfluidic chamber fabrication: A custom made acrylic top enclosure, polydimethylsiloxane (PDMS) gasket and bottom mount make up the flow channel assembly (see Supplementary Note 1). This allows the sample solution and DI water to flow across the sensor on the photonic chips, and doubles as a containment to allow a fixed volume of sample solution to stay atop the sensor for 120 s during ion interaction. The custom made PDMS gasket is fabricated by curing a PDMS and photo-initiator mixture (Shin-Etsu KER-4690) in polytetrafluoroethylene (PTFE) mold under 405 nm UV lamp for 10 minutes.

Analyte preparation: The analyte solution preparation is carried out by diluting 1000 ppm ICP standard solutions of the selected ions (Merck) with DI water to the concentration required; for low concentrations (lower than 10 ppm), multiple rounds of dilution were performed. ICP-MS is used to verify the concentrations.

Fundamental TE maintenance: The Pb^{2+} photonic sensor is designed for fundamental TE operation. Fundamental TE operation is crucial for the maintenance of interference fringes corresponding to the mode as well as fringe visibility. In order to ensure that the device is operating with only the fundamental TE mode, we utilized a chain of cascaded Multi-Mode Interferometer (MMI) structures that is optimized for the desired polarization ($10 \times \text{MMI}$). The polarization dependent loss the TM mode experience over TE is 2 dB per MMI. Cascading 10 MMIs yields a TM against TE polarization extinction ratio of 20 dB. By optimizing the input polarization corresponding to the maximum optical power at the output, we will be able to ensure that the device operates with only the fundamental TE mode.

Measurement of the calibration curve via a cumulative approach: The following is implemented for the measurement of the calibration curve. DI water was first added to obtain the reference wavelength (λ_0), and then flushed from the microfluidic chamber (Step 1). Next, DI water containing Pb^{2+} was added and held for 120 s to facilitate binding of Pb^{2+} to the functional surface at the sensing region (Step 2). The analyte was then removed again and DI

water is added, where the resonant wavelength is measured to remove the unbound species (Step 3). The optical transmission was subsequently measured. The shift in wavelength is determined by $\lambda_s - \lambda_0$. For the 6 concentrations that were measured (5, 25, 625, 2625, 62625, 262625 ppb), an additive approach was used. In Step 2, DI water containing 5, 20, 600, 2000, 60000, 200000 ppb of Pb^{2+} is added sequentially as the exposed concentration is increased. The measurement was repeated six times for each set of concentrations involving each photonic sensors, as indicated by the associated error bars in Fig. 5(b).

References

1. Hernberg, S. Lead poisoning in a historical perspective. *Am. J. Ind. Med.* **38** 244–254 (2000).
2. Lanphear, B. P., Rauch, S., Auinger, P., Allen, R. W. & Hornung, R. W. Low-level lead exposure and mortality in US adults: a population-based cohort study. *Lancet Public Health* **3**, e177–e184 (2018).
3. Guilarte, T. R., Toscano, C. D., McGlothan, J. L. & Weaver, S. A. Environmental enrichment reverses cognitive and molecular deficits induced by developmental lead exposure. *Ann. Neurol.* **53**, 50–56 (2003).
4. Gangoso, L. *et al.* Long-term effects of lead poisoning on bone mineralization in vultures exposed to ammunition sources. *Environ. Pollut.* **157**, 569–574 (2009).
5. Teerasantipan, T., Chaiteerakij, R., Prueksapanich, P. & Werawatganon, D. Changes in inflammatory cytokines, antioxidants and liver stiffness after chelation therapy in individuals with chronic lead poisoning. *BMC. Gastroenterol.* **20**, 263 (2020).
6. Lilis, R., Gavrilesco, N., Nestoresco, B., Dumitriu, C. & Roventa, A. Nephropathy in Chronic Lead Poisoning. *Occup. Environ. Med.* **25**, 196–202 (1968).
7. Dudev, T., Grauffel, C. & Lim, C. How Pb^{2+} Binds and Modulates Properties of Ca^{2+} -Signaling Proteins. *Inorg. Chem.* **57**, 14798–14809 (2018).
8. Cory-Slechta, D. A. Legacy of Lead Exposure: Consequences for the Central Nervous System. *Otolaryngol. Head Neck Surg.* **114**, 224–226 (1996).
9. Edwards, M. Fetal Death and Reduced Birth Rates Associated with Exposure to Lead-Contaminated Drinking Water. *Environ. Sci. Technol.* **48**, 739–746 (2014).
10. de Mattos, G. F., Costa, C., Savio, F., Alonso & Alonso, M. Lead poisoning: acute exposure of the heart to lead ions promotes changes in cardiac function and Cav1.2 ion channels. *Biophys. Rev.* **9**, 807–825 (2017).
11. Samarghandian, S. *et al.* A systematic review of clinical and laboratory findings of lead poisoning: lessons from case reports. *Toxicol. Appl. Pharmacol.* **429**, 115681 (2021).
12. Rothschild, E. O. Lead Poisoning — The Silent Epidemic. *N. Engl. J. Med.* **283**, 704–705 (1970).
13. Miracle, V. A. Lead Poisoning in Children and Adults. *Dimens. Crit. Care Nurs.* **36**, (2017).
14. Ahamed, M. & Siddiqui, M. K. J. Low level lead exposure and oxidative stress: Current opinions. *Clin. Chim. Acta* **383**, 57–64 (2007).
15. Boskabady, M. *et al.* The effect of environmental lead exposure on human health and the contribution of inflammatory mechanisms, a review. *Environ. Int.* **120**, 404–420 (2018).
16. Needleman, H. L. & Bellinger, D. The Health Effects of Low Level Exposure to Lead. *Annu. Rev. Public Health* **12**, 111–140 (1991).
17. THE WHITE HOUSE. FACT SHEET: The Biden-Harris Lead Pipe and Paint Action Plan. <https://www.whitehouse.gov/briefing-room/statements-releases/2021/12/16/fact-sheet-the-biden-harris-lead-pipe-and-paint-action-plan/> (2021).

18. Nicholas Rees & Richard Fuller. The Toxic Truth: Children's Exposure to Lead Pollution Undermines a Generation of Future Potential. <https://www.unicef.org/media/73246/file/The-toxic-truth-children's-exposure-to-lead-pollution-2020.pdf> (2020).
19. United States Environmental Protection Agency. Lead and Copper Rule. [https://www.google.com/search?client=safari&rls=en&q=Environmental+and+Energy+Law+Program+\(EPA\)%2C+US+has+implemented+a+limit+of+15+parts-per-billion+\(ppb\)+in+drinking+water&ie=UTF-8&oe=UTF-8&dlr=1&sei=PmIQZdm5KKulptQP7aCk8Aw](https://www.google.com/search?client=safari&rls=en&q=Environmental+and+Energy+Law+Program+(EPA)%2C+US+has+implemented+a+limit+of+15+parts-per-billion+(ppb)+in+drinking+water&ie=UTF-8&oe=UTF-8&dlr=1&sei=PmIQZdm5KKulptQP7aCk8Aw) (2022).
20. Perry Gottesfeld. The Environmental And Health Impacts Of Lead Battery Recycling. https://wedocs.unep.org/bitstream/handle/20.500.11822/13943/1_ECOWAS%20lead%20background%202016.pdf.
21. World Health Organization. Exposure to lead: a major public health concern, 2nd edition. <https://www.who.int/publications/i/item/9789240037656> (2021).
22. Almost 1 million people die every year due to lead poisoning, with more children suffering long-term health effects. <https://www.who.int/news/item/23-10-2022-almost-1-million-people-die-every-year-due-to-lead-poisoning--with-more-children-suffering-long-term-health-effects> (2022).
23. Meng, X. *et al.* A highly sensitive and selective chemosensor for Pb²⁺ based on quinoline–coumarin. *RSC Adv.* **8**, 33947–33951 (2018).
24. Yap, S. H. K. *et al.* An Advanced Hand-Held Microfiber-Based Sensor for Ultrasensitive Lead Ion Detection. *ACS Sens.* **3**, 2506–2512 (2018).
25. Kriss, R., Pieper, K. J., Parks, J. & Edwards, M. A. Challenges of Detecting Lead in Drinking Water Using at-Home Test Kits. *Environ. Sci. Technol.* **55**, 1964–1972 (2021).
26. Guo, J. *et al.* Crown ethers in graphene. *Nat. Commun.* **5**, 5389 (2014).
27. RUIZ-HITZKY, E. & CASAL, B. Crown ether intercalations with phyllosilicates. *Nature* **276**, 596–597 (1978).
28. Pedersen, C. J. The Discovery of Crown Ethers (Noble Lecture). *Angewandte Chemie International Edition in English* **27**, 1021–1027 (1988).
29. Pedersen, C. J. The Discovery of Crown Ethers. *Science (1979)* **241**, 536–540 (1988).
30. Pedersen, C. J. Cyclic polyethers and their complexes with metal salts. *J. Am. Chem. Soc.* **89**, 7017–7036 (1967).
31. Zhang, H. X. *et al.* Crown ether functionalized graphene oxide as ultrasensitive electrochemical sensor for detection of potassium ions. *Mater. Res. Express* **6**, 125095 (2019).
32. Iannazzo, D. *et al.* Electrochemical and Fluorescent Properties of Crown Ether Functionalized Graphene Quantum Dots for Potassium and Sodium Ions Detection. *Nanomaterials* **11**, (2021).
33. Kumbhat, S. & Singh, U. A potassium-selective electrochemical sensor based on crown-ether functionalized self assembled monolayer. *J. Electroanal. Chem.* **809**, 31–35 (2018).
34. Móczár, I. & Huszthy, P. Optically active crown ether-based fluorescent sensor molecules: A mini-review. *Chirality* **31**, 97–109 (2019).
35. Hsieh, Y.-C., Chir, J.-L., Wu, H.-H., Chang, P.-S. & Wu, A.-T. A sugar-aza-crown ether-based fluorescent sensor for Hg²⁺ and Cu²⁺. *Carbohydr. Res.* **344**, 2236–2239 (2009).
36. Kele, P., Orbulescu, J., Calhoun, T. L., Gawley, R. E. & Leblanc, R. M. Langmuir Monolayer and Langmuir–Blodgett Film Studies of an Amphiphilic Coumaryl Crown Ether. *Langmuir* **18**, 8523–8526 (2002).
37. Zhu, M., Lerum, M. Z. & Chen, W. How To Prepare Reproducible, Homogeneous, and Hydrolytically Stable Aminosilane-Derived Layers on Silica. *Langmuir* **28**, 416–423 (2012).
38. Howarter, J. A. & Youngblood, J. P. Optimization of Silica Silanization by 3-Aminopropyltriethoxysilane. *Langmuir* **22**, 11142–11147 (2006).
39. Khan, Z. *et al.* Current developments in esterification reaction: A review on process and parameters. *J. Ind. Eng. Chem.* **103**, 80–101 (2021).
40. Esteban, D. *et al.* Cadmium(II) and Lead(II) Complexes with Novel Macrocyclic Receptors Derived from 1,10-Diaza-15-crown-5. *Eur. J. Inorg. Chem.* **2000**, 1445–1456 (2000).
41. Wang, D.-M. *et al.* Polymer Gels Containing Dibenzo-24-Crown-8 Ether Moieties for Removal of Cesium Ions from Aqueous Environment. *Transactions of the Materials Research Society of Japan* **44**, 217–220 (2019).

42. Cooper, T. E., Carl, D. R., Oomens, J., Steill, J. D. & Armentrout, P. B. Infrared Spectroscopy of Divalent Zinc and Cadmium Crown Ether Systems. *J. Phys. Chem. A* **115**, 5408–5422 (2011).
43. Kumbhat, S. & Singh, U. A potassium-selective electrochemical sensor based on crown-ether functionalized self assembled monolayer. *J. Electroanal. Chem.* **809**, 31–35 (2018).
44. Ganjali, M. R., Moghimi, A. & Shamsipur, M. Beryllium-Selective Membrane Electrode Based on Benzo-9-crown-3. *Anal. Chem.* **70**, 5259–5263 (1998).
45. Gupta, V. K., Jain, A. K. & Kumar, P. PVC-based membranes of N,N'-dibenzyl-1,4,10,13-tetraoxa-7,16-diazacyclooctadecane as Pb(II)-selective sensor. *Sens. Actuators B Chem.* **120**, 259–265 (2006).
46. Abou, D. S. *et al.* Towards the stable chelation of radium for biomedical applications with an 18-membered macrocyclic ligand. *Chem. Sci.* **12**, 3733–3742 (2021).
47. Oral, I. & Abetz, V. Improved alkali metal ion capturing utilizing crown ether-based diblock copolymers in a sandwich-type complexation. *Soft Matter* **18**, 934–937 (2022).
48. Kazemi, S. Y. & Hamidi, A. S. Competitive Removal of Lead(II), Copper(II), and Cadmium(II) Ions through a Bulk Liquid Membrane Containing Macrocyclic Crown Ethers and Oleic Acid as Ion Carriers. *J. Chem. Eng. Data* **56**, 222–229 (2011).
49. Gatto, V. J. & Gokel, G. W. Syntheses of calcium-selective, substituted diaza-crown ethers: a novel, one-step formation of bibrachial lariat ethers (BiBLES). *J. Am. Chem. Soc.* **106**, 8240–8244 (1984).
50. Vaidya, B., Porter, M. D., Utterback, M. D. & Bartsch, R. A. Selective Determination of Cadmium in Water Using a Chromogenic Crown Ether in a Mixed Micellar Solution. *Anal. Chem.* **69**, 2688–2693 (1997).
51. Fahrenkopf, N. M. *et al.* The AIM Photonics MPW: A Highly Accessible Cutting Edge Technology for Rapid Prototyping of Photonic Integrated Circuits. *IEEE J. Sel. Top. Quantum Electron.* **25**, 1–6 (2019).
52. Sia, J. X. B. *et al.* Wafer-Scale Demonstration of Low-Loss (~0.43 dB/cm), High-Bandwidth (>38 GHz), Silicon Photonics Platform Operating at the C-Band. *IEEE Photonics J.* **14**, 1–9 (2022).
53. Rahim, A. *et al.* Open-Access Silicon Photonics Platforms in Europe. *IEEE J. Sel. Top. Quantum Electron.* **25**, 1–18 (2019).
54. Siew, S. Y. *et al.* Review of Silicon Photonics Technology and Platform Development. *J. Lightwave Technol.* **39**, 4374–4389 (2021).
55. Kohler, D. *et al.* Biophotonic sensors with integrated Si₃N₄-organic hybrid (SiNOH) lasers for point-of-care diagnostics. *Light Sci. Appl.* **10**, 64 (2021).
56. Luan, E., Shoman, H., Ratner, D. M., Cheung, K. C. & Chrostowski, L. Silicon Photonic Biosensors Using Label-Free Detection. *Sensors* **18**, (2018).
57. Zhang, H. *et al.* In Situ Regeneration of Silicon Microring Biosensors Coated with Parylene C. *Langmuir* **38**, 504–513 (2022).
58. Wang, X. *et al.* A silicon photonic biosensor using phase-shifted Bragg gratings in slot waveguide. *J. Biophotonics* **6**, 821–828 (2013).
59. Watanabe, K., Wu, H.-Y., Xavier, J., Joshi, L. T. & Vollmer, F. Single Virus Detection on Silicon Photonic Crystal Random Cavities. *Small* **18**, 2107597 (2022).
60. Liu, Q. *et al.* Highly sensitive Mach–Zehnder interferometer biosensor based on silicon nitride slot waveguide. *Sens. Actuators B Chem.* **188**, 681–688 (2013).
61. Claes, T. *et al.* Label-Free Biosensing With a Slot-Waveguide-Based Ring Resonator in Silicon on Insulator. *IEEE Photonics J.* **1**, 197–204 (2009).
62. Tu, X. *et al.* Thermal independent Silicon-Nitride slot waveguide biosensor with high sensitivity. *Opt. Express* **20**, 2640–2648 (2012).
63. Almeida, V. R., Xu, Q., Barrios, C. A. & Lipson, M. Guiding and confining light in void nanostructure. *Opt. Lett.* **29**, 1209–1211 (2004).
64. Kita, D. M., Michon, J., Johnson, S. G. & Hu, J. Are slot and sub-wavelength grating waveguides better than strip waveguides for sensing? *Optica* **5**, 1046–1054 (2018).
65. Palmer, R. *et al.* Low-Loss Silicon Strip-to-Slot Mode Converters. *IEEE Photonics J.* **5**, 2200409 (2013).

66. Sia, J. X. B. *et al.* Mid-Infrared, Ultra-Broadband, Low-Loss, Compact Arbitrary Power Splitter Based on Adiabatic Mode Evolution. *IEEE Photonics J.* **11**, 1–11 (2019).
67. Puumala, L. S. *et al.* An Optimization Framework for Silicon Photonic Evanescent-Field Biosensors Using Sub-Wavelength Gratings. *Biosensors (Basel)* **12**, (2022).
68. Casas, A., Ramos, M. J., Rodríguez, J. F. & Pérez, Á. Tin compounds as Lewis acid catalysts for esterification and transesterification of acid vegetable oils. *Fuel Process. Technol.* **106**, 321–325 (2013).
69. Fischer, M. J. E. Amine Coupling Through EDC/NHS: A Practical Approach. in *Surface Plasmon Resonance: Methods and Protocols* (ed. Mol Nico J. and Fischer, M. J. E.) 55–73 (Humana Press, 2010). doi:10.1007/978-1-60761-670-2_3.
70. Stefan Hüfner. *Photoelectron Spectroscopy Principles and Applications*. vol. 82 (Springer-Verlag Berlin Heidelberg New York, 2003).
71. Aris, A. Z., Kam, R. C. Y., Lim, A. P. & Praveena, S. M. Concentration of ions in selected bottled water samples sold in Malaysia. *Appl. Water Sci.* **3**, 67–75 (2013).
72. Vu, H., Merkel, B. & Wiche, O. Major ions, trace elements and evidence of groundwater contamination in Hanoi, Vietnam. *Environ. Earth Sci.* **81**, 305 (2022).
73. Abd Elnabi, M. K. *et al.* Toxicity of Heavy Metals and Recent Advances in Their Removal: A Review. *Toxics* **11**, (2023).
74. Liu, Y., Lotero, E. & Goodwin, J. G. Effect of water on sulfuric acid catalyzed esterification. *J. Mol. Catal. A Chem.* **245**, 132–140 (2006).
75. da Silva, M. J., Julio, A. A. & dos Santos, K. T. Sn(ii)-catalyzed β -citronellol esterification: a Brønsted acid-free process for synthesis of fragrances at room temperature. *Catal. Sci. Technol.* **5**, 1261–1266 (2015).
76. Xie, W., Wang, H. & Li, H. Silica-Supported Tin Oxides as Heterogeneous Acid Catalysts for Transesterification of Soybean Oil with Methanol. *Ind. Eng. Chem. Res.* **51**, 225–231 (2012).
77. Baek, H., Minakawa, M., Yamada, Y. M. A., Han, J. W. & Uozumi, Y. In-Water and Neat Batch and Continuous-Flow Direct Esterification and Transesterification by a Porous Polymeric Acid Catalyst. *Sci. Rep.* **6**, 25925 (2016).
78. Buttersack, C. Modeling of type IV and V sigmoidal adsorption isotherms. *Phys. Chem. Chem. Phys.* **21**, 5614–5626 (2019).
79. Altun, A. O., Bond, T., Pronk, W. & Park, H. G. Sensitive Detection of Competitive Molecular Adsorption by Surface-Enhanced Raman Spectroscopy. *Langmuir* **33**, 6999–7006 (2017).

Data Availability

The datasets generated and analyzed in the current study are available from the corresponding authors upon reasonable request.

Acknowledgements

Jia Xu Brian Sia would like to acknowledge Ministry of Education/NTU College of Engineering International Postdoctoral Fellowship. This work was performed in part through the use of the facilities of MIT.nano, Harvard University Center for Nanoscale Systems (CNS), NTU's Centre for Micro- & Nano-Electronics (CMNE) and Nanyang Nanofabrication Centre (N2FC). The authors also wish to acknowledge this collaborative work with Fingate Technologies and Vulcan Photonics.

Author Contribution

J. X. B. S., L. R., Y. Z. T. conceived the idea to integrate crown ethers with silicon photonics for ion detection with the help from C. S. O., X. G., K. N. K., X. L., W. W., S. S., C. L., R., C. G. L., G. T. R., J. J. H., H. W.. Y. Z. T. conceived the functionalization process flow. L. R. did the photonic design and fabrication. X. G. did the photonic sensor characterization. K. N. K. did the material characterization with the help from Y. Z. T. and C. S. O.. Y. Z. T. and G. X. designed and constructed the sensor assembly. L. R., Y. Z. T., J. J. H. and J. X. B. S. wrote the manuscript with inputs from C. S. O, X. G., K. N. K., X. L., W. W., S. S., C. L., R., C. G. L., G. T. R., H. W.. J. X. B. S., H. W. and J. J. H. supervised the project.

Competing Interests

Yong Zen Tan, Chi Siang Ong and Khong Nee Koo have filed patent applications on the chemical synthesis methods and sensor design described in the manuscript. Vulcan Photonics is working on the commercialization of the photonic sensors described in the manuscript. The remaining authors declare no competing interests.

Figure Legends

Fig. 1 Concept of the Crown Ether/SiP platform for ion detection. **a**, 3-D illustration of the photonic Pb^{2+} ion sensor based on the crown ether decorated SiP platform. The functionalization performed in the sensing arm is indicated by the features in red, where the inset illustrates the crown ether functionalized to the Si/SiO₂ surface by Fischer esterification, and then amine conjugation. **b**, The micrograph image of the Pb^{2+} ion sensor, where the sensing arm and scale bar (500 μm) are indicated. **c**, Elucidated operating principle of the photonic Pb^{2+} ion sensor. The inset shows the exemplary applications that the ion detection platform can be extended to. **d**, The Pb^{2+} photonic sensor assembly, consisting of the photonic chip and a microfluidic chamber.

Fig. 2 Photonic design of the lead ion sensor **a**, Simulation of the number of supported TE optical modes in the slot waveguides as a function of strip and slot width. **b**, Sensor surface sensing FoM as a function of strip and slot width. **c**, The comparison of two proposed splitting Mach-Zehnder architectures (see Supplementary Note 3) in terms of the power asymmetry required of the splitter; condition 1 ($S_1 = S_2, S'_1 = S'_2, S'_{1/2} \neq 0.5$), condition 2

($S'_1 \neq 0.5, S'_2 = 0.5$). Top-down electric field distribution of the **d**, asymmetrical adiabatic tapered splitter, and **e**, adiabatic strip-slot converter, where the structure of the components are outlined.

Fig. 3 The development of the Crown Ether/SiP functionalization process a, The developed crown ether/SiP functionalization process, described in 4 steps. XPS narrow spectra analysis of the **b**, N 1S, **c**, C 1S, **d**, O 1S regions of the photonic chips, before and after functionalization.

Fig. 4 Analysis of functional layer selectivity via XPS. Normalized narrow scan XPS spectra at photonic chip surface by subtracting the spectra prior to ion interaction from that of after ion interaction **a**, Na^+ , **b**, K^+ , **c**, Mg^+ , **d**, Li^+ , **e**, Zn^{2+} , **f**, Ca^{2+} , **g**, Fe^{2+} , **h**, Cu^{2+} , **i**, Al^{3+} , **j**, Sn^{2+} , **k**, Cd^{2+} , and **l**, Pb^{2+} ions respectively.

Fig. 5. Experimental characterization of Pb^{2+} sensor performance. a, Wavelength spectrum of the sensor, when DI water is applied into the sensor assembly (as shown in Fig. 1c). **b**, Calibration curve of the sensor when exposed to Pb^{2+} concentration of 0, 5, 25, 125, 625, 2625, 12625, 62625, 262625 ppb, via a cumulative testing approach (see Experimental Section). **c**, A set of fringe minima corresponding to the tested concentration in the calibration curve (Fig. 5b). **d**, Fig. 5c, zoomed-in at concentrations of 0, 5, 25 ppb. Validation of the calibration curve (Fig. 5b) at concentrations of **e**, 80, **f**. 10 and **g**, 1 ppb.

Fig. 6. Selectivity performance of the Pb^{2+} ion photonic sensor against a, Cd^{2+} , and **b**, K^+ at 15 ppb where no shifts in the interferometric spectra indicative of ion binding is observed. Similar to Fig. 5 e-g, the detection performance of the Pb^{2+} photonic ion sensor is tested at 15 ppb, where significant ion binding, resulting in interferometric shifts that corresponds closely to Fig. 5b is observed.

Supplementary Fig. 1. Exploded view representation of the Pb^{2+} ion sensor assembly, consisting of the bottom mount, photonic chip, PDMS gasket, acrylic top enclosure, and the screws, which are used to secure the assembly, and prevent microfluidic chamber leakage. The assembly is mounted on top of a TEC controller for thermal stabilization.

Supplementary Fig. 2. Definition of FoM for the optimization of waveguide surface sensitivity. The height of the waveguide layer is 220 nm with a 20 nm SiO_2 layer surrounding the waveguide, deposited via ALD.

a, Cross-sectional schematic of the slot waveguide with definition of slot and strip width illustrated; the area of confinement is illustrated. **b**, An instance of electric field distribution pertaining to a slot waveguide with slot and strip width of 240 nm. **c**, Cross-sectional schematic of the strip waveguide(TE/TM) with definition of strip width illustrated; the area of confinement is illustrated. **d**, Sensor surface sensing FoM for strip waveguides (TE and TM) as a function of strip width. Instances of electric field distribution pertaining to **e**, TE strip waveguide with width of 270 nm, and **f**, TM strip waveguide with width of 425 nm.

Supplementary Fig 3. Architectures of two MZI-based sensor designs with a, Condition 1, $S_1 = S_2, S'_1 = S'_2, S_{1/2} = 1 - S'_{1/2}$, where $S'_{1/2} \neq 0.5$, and **b**, Condition 2, $S_{1/2} = 1 - S'_{1/2}$, where $S'_1 \neq 0.5$, and $S'_2 = 0.5$.

According to Fig. 2c of the main text, it can be seen that the architecture in Supplementary Fig. 2a, condition 1 imposes lower requirements on splitter asymmetry as compared to Supplementary Fig. 2b, condition 2.

Supplementary Fig. 4 EDX analysis of the photonic chips pertaining to Si, N, C, O, and Pb elemental composition a, prior functionalization, **b**, after functionalization, and **c**, after Pb^{2+} exposure and rinse with DI water and dry (N_2).

Supplementary Fig. 5 XPS spectrum measured after dilute nitric acid purification and prior to Sn^{2+} exposure, and after Sn exposure with DI water rinse and dry (N_2).

Supplementary Fig. 6. Measured optical spectrum of the photonic sensor when the sensing region of the photonic sensor is exposed to air. Poor visibility, as implied from the interferometric spectrum ER is observed, which is resultant when the designed losses are non-optimal to the asymmetrical splitting ratios.

Supplementary Fig. 7 The SEM image (false colour) of fabricated slot waveguide, with strip and slot widths of 240 nm.

Supplementary Fig. 8 Selectivity performance of the Pb^{2+} ion sensor against a, Na^+ , **b**, Mg^+ , **c**, Cu^+ , **d**, Sn^{+2} , **e**, Ca^{+2} , **f**, Fe^{+2} at 15 ppb where no shifts in the interferometric spectra indicative of ion binding is observed across all the tested ions.

Supporting Information

Crown ether decorated silicon photonics for safeguarding against lead poisoning

Luigi Ranno^{1,†}, Yong Zen Tan^{2,†}, Chi Siang Ong², Xin Guo³, Khong Nee Koo⁴, Xiang Li³, Wanjun Wang³, Samuel Serna¹, Chongyang Liu⁵, Rusli³, Callum G. Littlejohns⁶, Graham T. Reed⁶, Juejun Hu¹, Hong Wang³ and Jia Xu Brian Sia^{1,3,*}

¹*Department of Materials Science & Engineering, Massachusetts Institute of Technology, Cambridge, M.A., USA*

²*Fingate Technologies, Singapore*

³*School of Electrical and Electronic Engineering, Nanyang Technological University, 50 Nanyang Avenue, 639798, Singapore*

⁴*Vulcan Photonics, Kuala Lumpur, Malaysia*

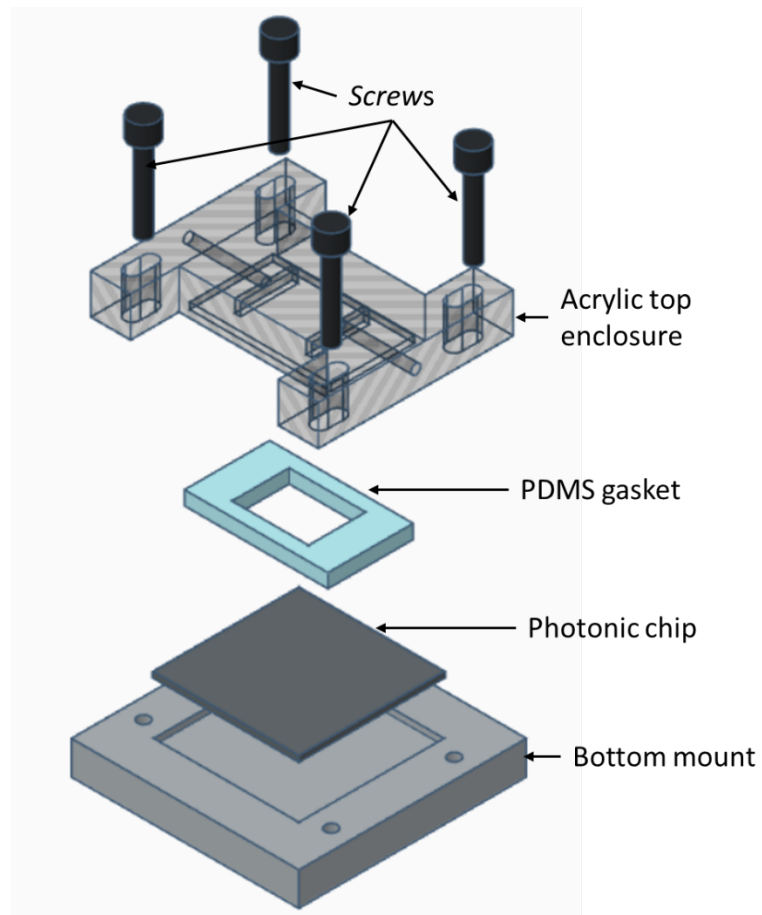
⁵*Temasek Laboratories, Nanyang Technological University, 50 Nanyang Avenue, 637553, Singapore*

⁶*Optoelectronics Research Centre, University of Southampton, Southampton SO17 1BJ, UK*

[†]*These authors contributed equally*

**Corresponding author: jxbsia@mit.edu, jiaxubrian.sia@ntu.edu.sg*

Supplementary Note 1: Exploded-view schematic representation of the Pb²⁺ ion sensor assembly



Supplementary Fig. 1. Exploded view representation of the Pb²⁺ ion sensor assembly, consisting of the bottom mount, photonic chip, PDMS gasket, acrylic top enclosure, and the screws, which are used to secure the assembly, and prevent microfluidic chamber leakage. The assembly is mounted on top of a TEC controller for thermal stabilization.

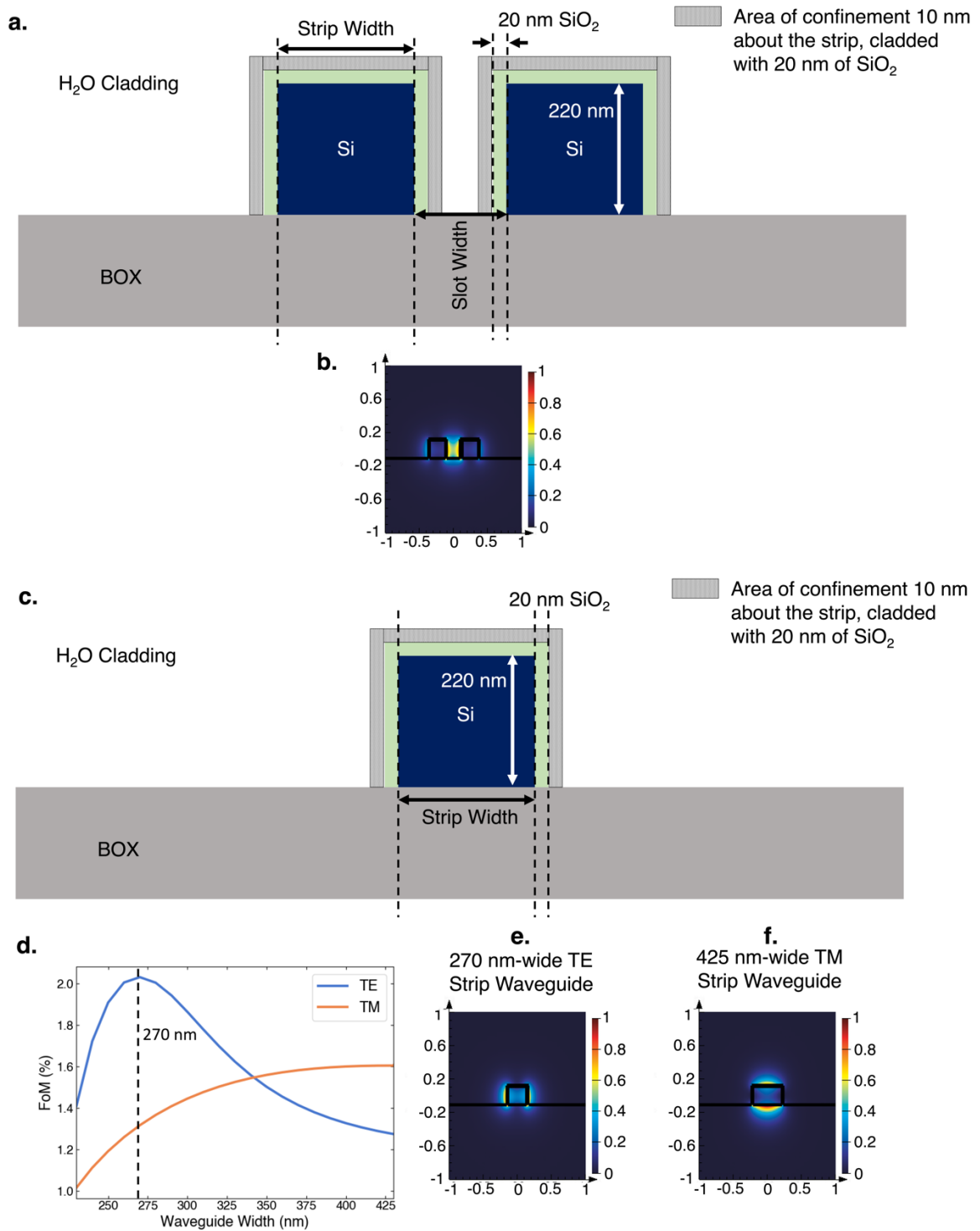
Supplementary Note 2: Definition of FoM for the Optimization of Surface Sensitivity

The cross section of a slot waveguide is illustrated in Supplementary Fig. 2a, with strip and slot width indicated; 20 nm of SiO₂ is deposited on the strip via ALD prior functionalization (Fig. 3a of the main text). For instance, the electric field distribution of the implemented slot waveguide with strip and slot width of 240 nm is shown in Supplementary Fig. 2b. Higher surface sensitivity implies that power of the optical mode about the surface of the strip width will be higher. To that effect, the FoM which considers the confinement factor 10 nm from the waveguide surface, with 20 nm of SiO₂ cladding, is derived from the following:

$$FoM = \frac{\partial n_{eff.}}{\partial n_{confine}} = \frac{n_g}{n_{confine}} \frac{\int_{confine} \epsilon |\vec{E}|^2 dA}{\int \epsilon |\vec{E}|^2 dA} \quad (2.1)$$

$n_{eff.}$ and n_g are the effective index and group index of the optical mode respectively, \vec{E} is the electric field of the waveguide mode, $n_{confine}$ and ϵ are the material index and the dielectric permittivity of the medium. In the computation, the medium surrounding the waveguide is taken to be water. The 2D integral in the numerator is to be taken about the 10 nm region which surrounds the waveguide and its cladding, while the integral at the denominator is considered about the entire space. The computed FoM of the slot waveguide is indicated in Fig. 2b of the main text. It is known that when the slot width is comparable to the exponential decay length of the fundamental eigenmode, optical power perpendicular to the high-index contrast interfaces is amplified¹⁻⁶. As a comparison, the optical power 10 nm about the surface of strip TE and TM waveguides with 20 nm of SiO₂ cladding was also computed. The cross section of the strip waveguide is illustrated in Supplementary Fig. 2c. The FoM of the strip waveguides at the fundamental TE and TM polarization are computed as a function of strip widths in Supplementary Fig. 2d. On the 220 nm SOI platform, at $\lambda = 1.55 \mu\text{m}$, the optimal waveguide width for surface sensing at the TE polarization is found to be 270 nm. The FoM for TM strip waveguides is found to be lower than that of TE. This is because for TM polarization, the

optical field is intensified at the top and bottom interfaces of the waveguide (Supplementary Fig. 2f)⁷, unlike TE (Supplementary Fig. 2e), which is lateral⁷. The field at the bottom interface of the TM waveguide does not contribute to surface sensitivity. Furthermore, as the BOX has higher material refractive index than DI water, the field intensity at the bottom interface of the TM strip waveguide will be higher than that at the top (Supplementary Fig. 2f). From Supplementary Fig. 2d it can be seen that the FoM of the TM strip waveguide plateaus when strip width is larger 400 nm; the cross sectional electric field distribution of a TM strip waveguide with width of 425 nm is indicated in Supplementary Fig. 2f. Comparing the FoM of the slot waveguides (Fig. 2b of the main text) against that of the TE and TM slot waveguides, it can be seen that significantly higher surface sensitivity can be realized for slot waveguides. To that effect, slot waveguides are implemented for the Pb²⁺ photonic sensor presented in this work.

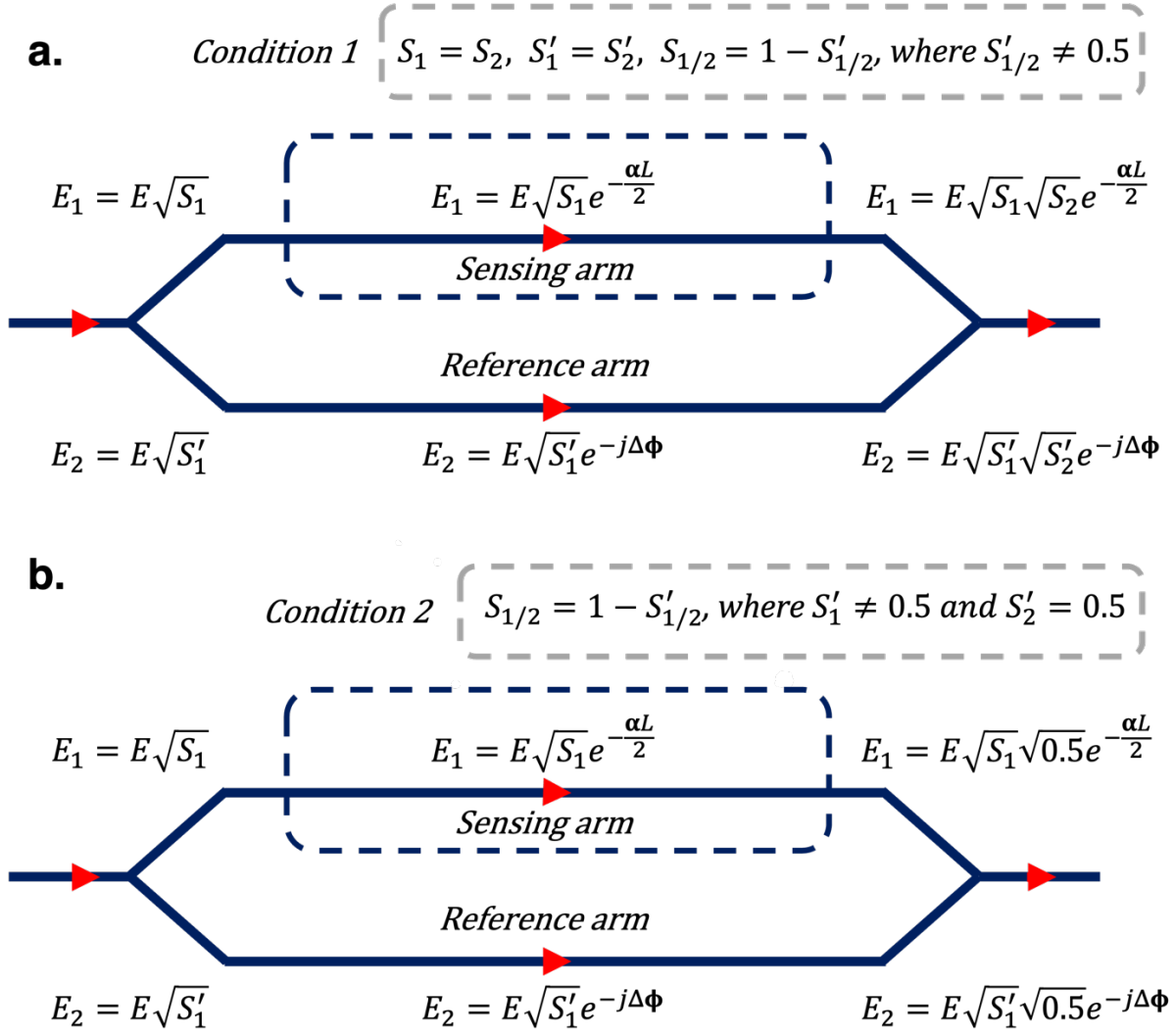


Supplementary Fig. 2. Definition of FoM for the optimization of waveguide surface sensitivity. The height of the waveguide layer is 220 nm with a 20 nm SiO₂ layer surrounding the waveguide, deposited via ALD. a, Cross-sectional schematic of the slot waveguide with definition of slot and strip width illustrated; the area of confinement is illustrated. b, An instance of electric field distribution pertaining to a slot waveguide with slot and strip width of 240 nm. c, Cross-sectional schematic of the strip waveguide (TE/TM) with definition of strip width

illustrated; the area of confinement is illustrated. **d**, Sensor surface sensing FoM for strip waveguides (TE and TM) as a function of strip width. Instances of electric field distribution pertaining to **e**, TE strip waveguide with width of 270 nm, and **f**, TM strip waveguide with width of 425 nm.

Supplementary Note 3: Derivation of Equation 3 in the main text, relating designed loss (water absorption) with splitter power ratios

Condition 1 is illustrated in Supplementary Fig. 3a. A lightwave ($I = |E^2|$) is injected into an asymmetrical splitters, with two power splitting ratios; S_1, S'_1 (input splitter) and S_2, S'_2 (output splitter) where, $S_1 = S_2$ and $S'_1 = S'_2, S'_{1/2} \neq 0.5$. Assuming the splitters are lossless, energy conservation dictates that $S_{1/2} = 1 - S'_{1/2}$. After the input splitter, the field is separated into the sensing and reference arm, yielding E_1 and E_2 respectively. These two terms are related to the electric field at the input of the splitter (E) through the splitting ratio such that $E_1 = E\sqrt{S_1}$ and $E_2 = E\sqrt{S'_1}$. As the light propagates through the sensing arm, it will accumulate attenuation from water absorption which we define as $e^{-\alpha L}$, with L being the sensing arm length and α is the attenuation constant, as compared to the reference arm. We can express the phase difference between the two MZI arms as $e^{-j\Delta\phi}$.



Supplementary Fig 3. Architectures of two MZI-based sensor designs with a, Condition 1, $S_1 = S_2, S'_1 = S'_2, S_{1/2} = 1 - S'_{1/2}$, where $S'_{1/2} \neq 0.5$, and b, Condition 2, $S_{1/2} = 1 - S'_{1/2}$, where $S'_1 \neq 0.5$, and $S'_2 = 0.5$.

According to Fig. 2c of the main text, it can be seen that the architecture in Supplementary Fig. 2a, condition 1 imposes lower requirements on splitter asymmetry as compared to Supplementary Fig. 2b, condition 2.

Lastly, as the two fields recombine at the output splitter, the total output intensity will be of the form:

$$I_{out} = E^2 |\sqrt{S_1}\sqrt{S_2}e^{-\frac{\alpha L}{2}} + \sqrt{S'_1}\sqrt{S'_2}e^{-j\Delta\Phi}|^2 \quad (3.1)$$

In order to maximize sensor visibility, $I_{out} = 0$ during destructive interference condition. As a result, (S2.1) can be reduced to the following form,

$$\sqrt{S_1}\sqrt{S_2}e^{-\frac{\alpha L}{2}} = \sqrt{S'_1}\sqrt{S'_2} \quad (3.2)$$

An alternative MZI architecture (condition 2) is also illustrated in Supplementary Fig. 3b. In this design, an arbitrary and 3-dB splitter are used at the input and output respectively; $S'_1 \neq 0.5$, $S'_2 = 0.5$. The output of the MZI can be defined as the following.

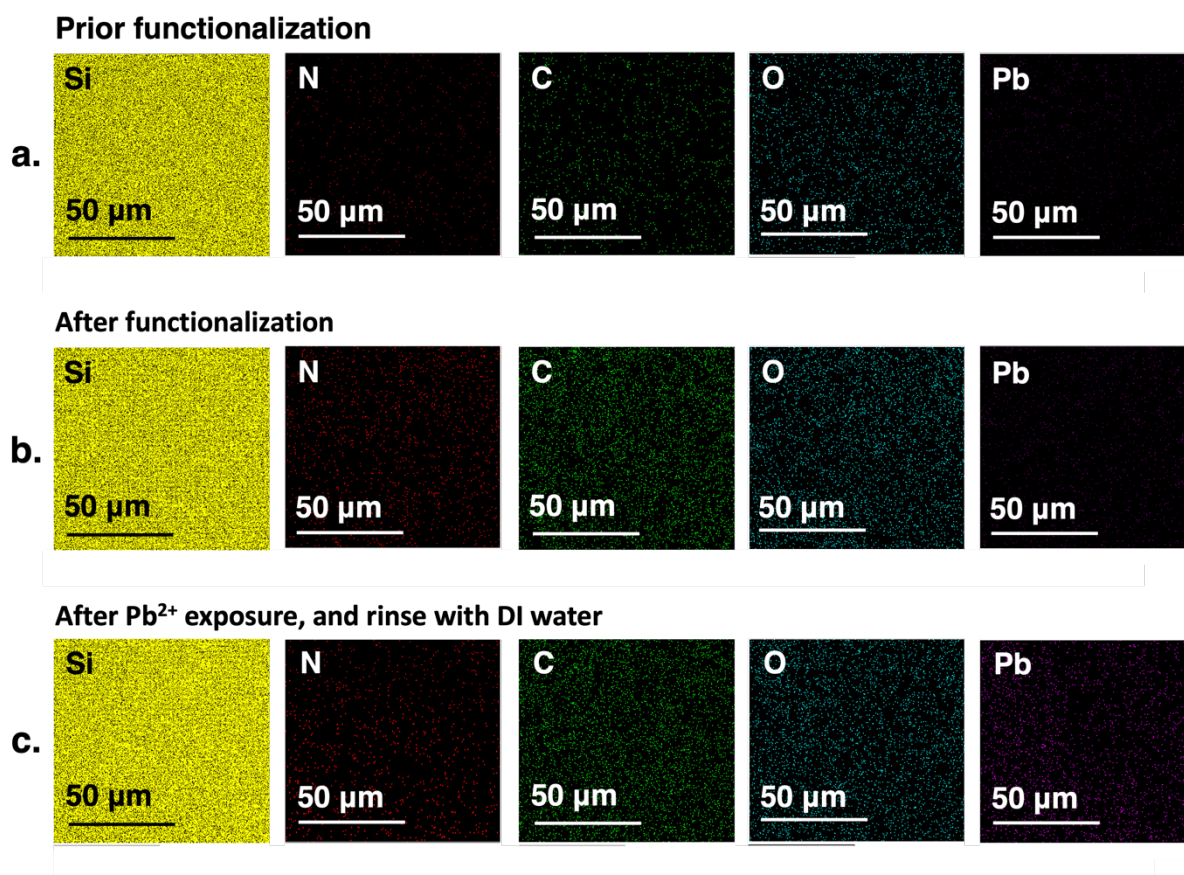
$$I_{out} = E^2 |\sqrt{S_1} \sqrt{0.5} e^{-\frac{\alpha L}{2}} + \sqrt{S'_1} \sqrt{0.5} e^{-j\Delta\phi}|^2 \quad (3.3)$$

Similarly, to maximize sensor visibility, we set $I_{out} = 0$. As such, Equation 3.3 can be reduced to.

$$\sqrt{S_1} e^{-\frac{\alpha L}{2}} = \sqrt{S'_1} \quad (3.4)$$

Via Equation 3.2 and 3.4, we determine the splitting ratio of the arbitrary splitters as a function of designed losses for the MZI architectures in Supplementary Fig. 3a-b; designed loss from water absorption is assumed to be the only source of optical loss. It can be seen that the MZI structure illustrated in Supplementary Fig. 3a reduces the asymmetrical requirement in power splitting which significantly alleviates requirement on fabrication ratios; accurate fabrication of highly asymmetrical power splitters is challenging; small variations in splitter dimensions will result in significant changes from the intended design.

Supplementary Note 4: Detection of Sn^{2+} through EDX analysis after functionalization

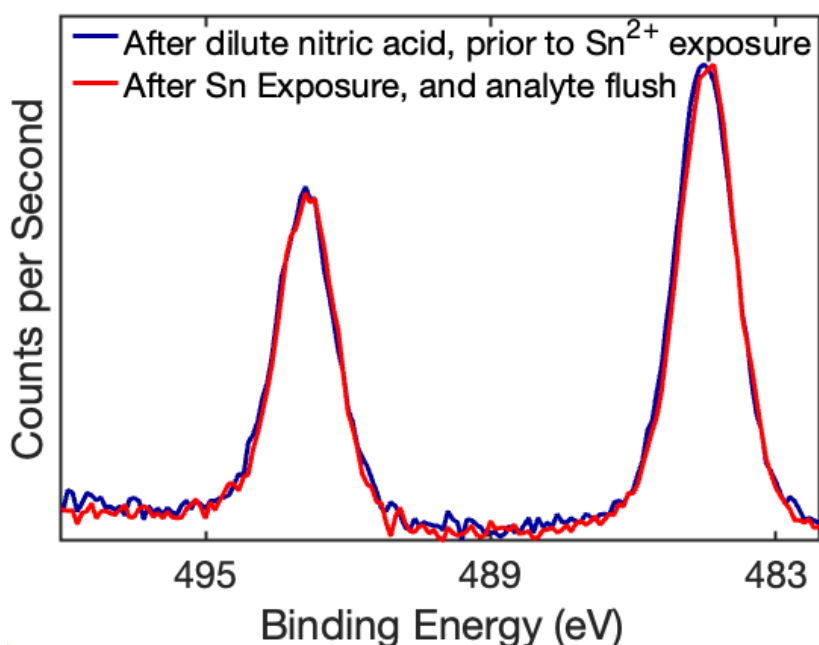


Supplementary Fig. 4 EDX analysis of the photonic chips pertaining to Si, N, C, O, and Pb elemental composition **a**, prior functionalization, **b**, after functionalization, and **c**, after Pb^{2+} exposure and rinse with DI water and dry (N_2).

In addition to the XPS results shown in the Fig. 3b-d, and Fig. 4I of the main text, an EDX analysis (Supplementary Fig. 4) was carried out to evaluate the elemental composition of Si, N, C, O and Pb. The analysis of N, C, and O indicates the viability of the Fischer esterification protocol that was developed in this work⁸. By comparing Supplementary Fig. 4a with Supplementary Fig. 4b or Supplementary Fig. 4c, an increase in N and C elemental composition can be observed. This is in line with the conclusion derived from the N 1S and C 1S regions of the XPS spectrums shown in Fig. 3b-c of the main text. We were not able to observe a change in O elemental composition in the EDX analysis. This is due to the fact that the O signal is attributed from the functional layer, as well as the 20 nm SiO_2 that was deposited on the slot

waveguides prior functionalization. As the 20 nm SiO₂ layer is the primary contributor to the O signal in Supplementary Fig. 4⁹, a clear change in signal intensity cannot be seen. To further validate the capacity of the functional layer to bind with Pb²⁺ ions, the functional layer is exposed to Pb²⁺ for 120 s, followed by flushing with DI water and drying (N₂). By comparing the rightmost column of Supplementary Fig. 4b and c, the appearance of Pb via the binding capabilities of the functional layer can be clearly observed.

Supplementary Note 5: Detection of Sn²⁺ through XPS analysis after functionalization

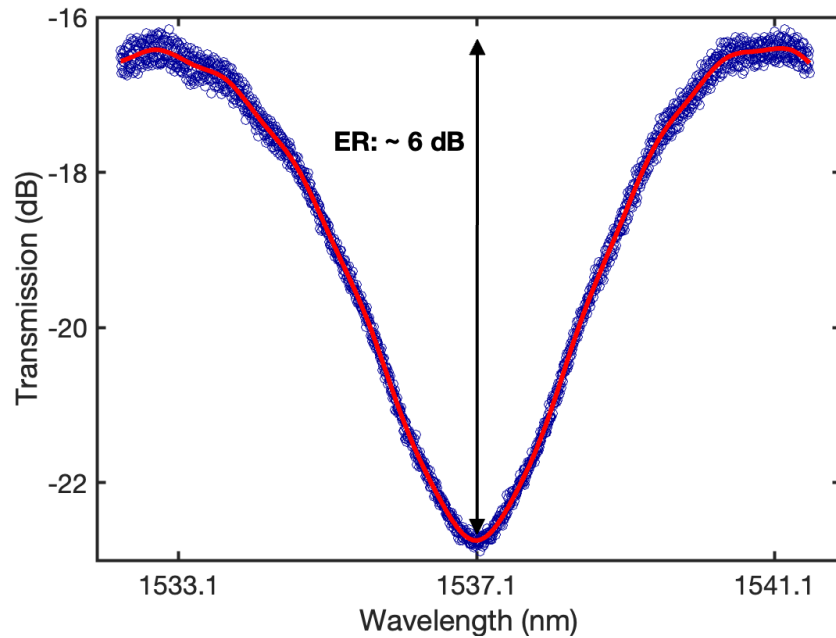


Supplementary Fig. 5 XPS spectrum measured after dilute nitric acid purification and prior to Sn²⁺ exposure, and after Sn exposure with DI water rinse and dry (N₂).

Due to the application of H₂O as a green solvent for the developed reaction, Brønsted acid catalyst such as H₂SO₄ is incompatible, in view of its drastic decrease in catalytic activity, in the presence of H₂O¹⁰. To that effect, the Lewis acid catalyst, SnCl₂ is utilized, which has a catalytic activity that is more resilient to the presence of H₂O^{11,12}. While Fischer esterification is favored when H₂O is removed as the reaction proceeds (dehydrative esterification), for the reaction disclosed in this work, Sn is embedded within the SiO₂ substrate, forming a

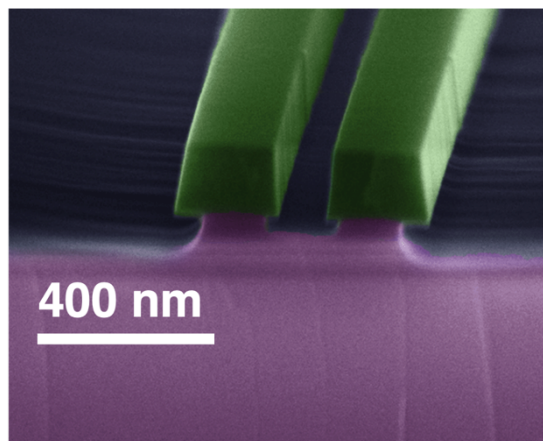
heterogeneous catalyst. Thereby, improved catalytic activity¹³ that favors esterification in the presence of H₂O is achieved¹⁴. Evidence of successful Fischer esterification is indicated by the XPS N 1S, C 1S, and O 1S data in Fig. 3b-d of the main text respectively, and the EDX analysis in Fig S4 (See Section S4 in Supporting Information). Furthermore, Supplementary Fig. 5 shows the XPS results of the functional layer after dilute nitric acid purification (process in Fig. 3a of the main text), prior to Sn²⁺ exposure. It can be seen that presence of Sn cannot be eliminated via the purification step. We note that heterogeneous catalyst displays improved catalytic activity that favors esterification, even in the presence of H₂O. Supplementary Fig. 5 also shows the XPS measurement of the functional layer after Sn²⁺ exposure, followed by DI water flush and drying. As the DBTA crown ethers that undergoes amine conjugation subsequently do not bind to Sn²⁺ ions, it can be seen that the XPS spectrum is similar to that prior Sn²⁺ exposure. The subtraction of the narrow scan XPS spectrum before ion interaction was subtracted to that after ion interaction, referring to the normalized XPS spectrum as shown in Fig. 5 of the main text.

Supplementary Note 6: Measured optical spectrum of the photonic sensor when the sensing region is exposed to air



Supplementary Fig. 6. Measured optical spectrum of the photonic sensor when the sensing region of the photonic sensor is exposed to air. Poor visibility, as implied from the interferometric spectrum ER is observed, which is resultant when the designed losses are non-optimal to the asymmetrical splitting ratios.

Supplementary Note 7: Details on chip fabrication

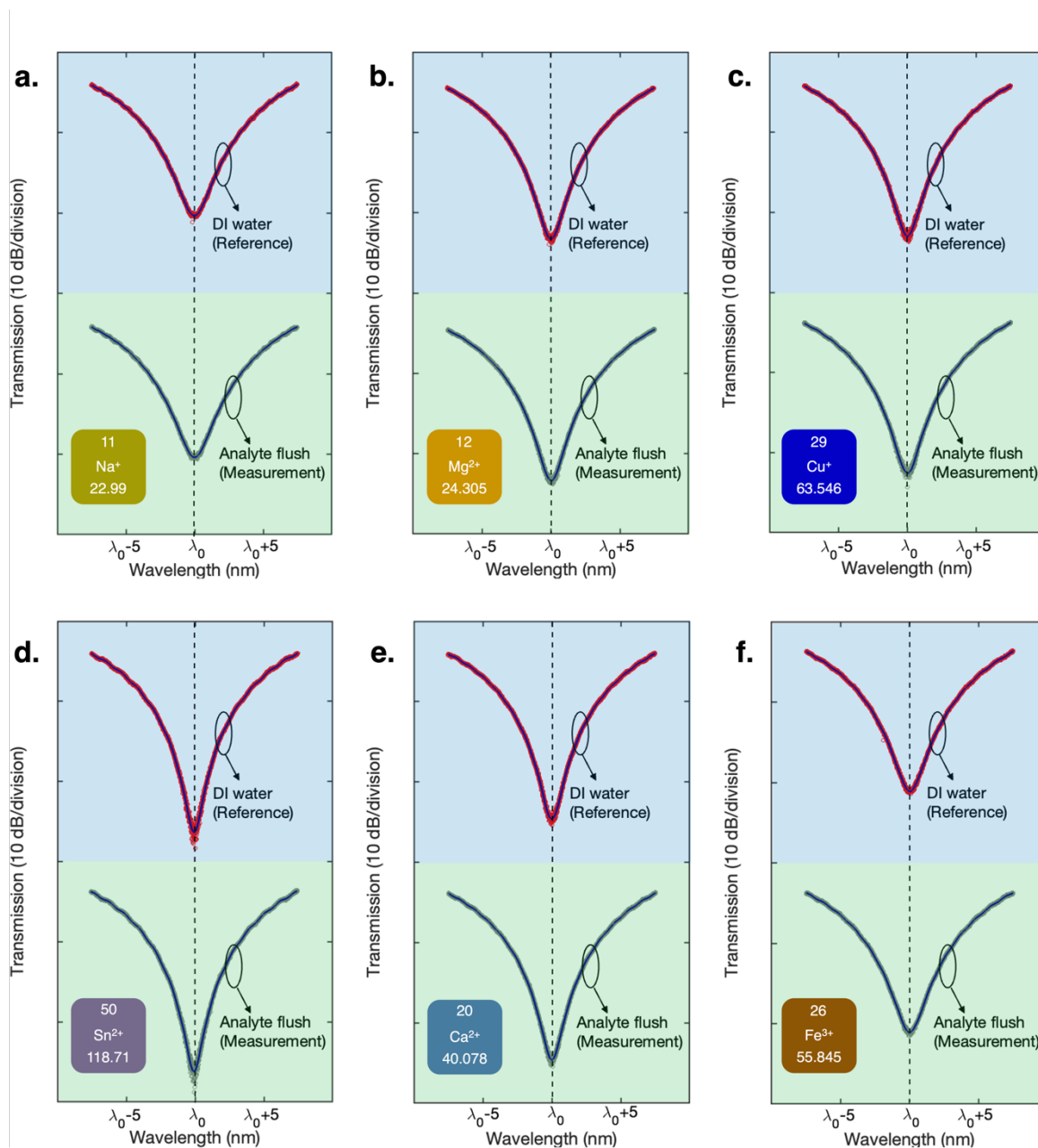


Supplementary Fig. 7 The SEM image (false colour) of fabricated slot waveguide, with strip and slot widths of 240 nm.

The fabrication of the sensor chips starts from commercially available 200 mm silicon on insulator wafers with 3 μm thick buried oxide and 220 nm thick device layer. First, the wafers are cleaned using a heated acetone bath kept at 55°C and rinsed in methanol, isopropanol and DI water. Then, an adhesion promoter (Surpass 4000) and electron-sensitive resist (ma-N 2403) are spin-coated onto the wafer and baked for 2 minutes at 90°C. The thickness of the E-beam resist after spin coating is \sim 300 nm (achieved at spin speeds of 3000 rounds per minute). A discharging layer (Espacer-300Z from Showa Denko Inc.) is applied to minimize charging effects. The wafer is patterned using E-beam lithography (ELS-HS50 from STS-Elionix) with a 50 kV accelerating voltage and a beam current of 5 nA. After development in RD6 (Futurexx Inc.) for 80s and rinsing in DI water, the waveguides are etched using ICP-RIE (RIE-230iP from Samco Inc.) with a gas chemistry of CF_4 and Ar at a pressure of 1 Pa, ICP Power of 300 W and 100 W of bias Power. The wafer is then ashed in O_2 plasma to strip away any remaining E-beam resist and to remove residual fluoropolymer formed during the etching process and thoroughly cleaned in Piranha solution, followed by a DI water rinse. Subsequently, the wafer was cladded with 2 μm of SiO_2 deposited at 350°C via PECVD (Samco PD-220NL from Samco Inc). The wafer was then baked at 115 °C and silanized in an oven (TA Series from Yield Engineering Systems Inc.) to increase adhesion promotion of photoresist. Then, a thin (\sim 1 μm) AZ 3312 photoresist layer is spin-coated and softbaked at 110°C for 60s. The sensing trench pattern is exposed into the resist using a maskless aligner (MLA-150 from Heidelberg Instruments Mikrotechnik GmbH) with a laser source centered at 405 nm. The resist was then post-exposure baked at 110 °C for 60 s and developed using AZ 726 MIF developer (Microchemicals GmbH) for 60 s. A diluted buffered oxide etchant solution was then used to open the sensing trenches, exposing the waveguides in the sensing arm. To avoid overetching, which could suspend the waveguides and generally change the structural cross-section from the intended design, the etching depth was monitored during the etching process using both

profilometry (Dektak-XT from Bruker Corporation) and reflectometry (F50-UVX from Filmetrics Inc.). Once a total etch depth of 2 μm is reached, the resist was stripped in oxygen plasma (e3511 wafer asher from ESI Inc.), followed by thorough cleaning in acetone, isopropanol and DI water to prepare the wafer for the crown ether functionalization step.

Supplementary Note 8 Pb^{2+} ion photonic sensor selectivity test against Na^+ , Mg^+ , Cu^+ , Sn^{+2} , Ca^{+2} , Fe^{2+}



Supplementary Fig. 8 Selectivity performance of the Pb⁺² ion sensor against a, Na⁺, b, Mg⁺, c, Cu⁺, d, Sn⁺², e, Ca⁺², f, Fe⁺² at 15 ppb where no shifts in the interferometric spectra indicative of ion binding is observed across all the tested ions.

References

1. Almeida, V. R., Xu, Q., Barrios, C. A. & Lipson, M. Guiding and confining light in void nanostructure. *Opt. Lett.* 29, 1209–1211 (2004).
2. Kita, D. M., Michon, J., Johnson, S. G. & Hu, J. Are slot and sub-wavelength grating waveguides better than strip waveguides for sensing? *Optica* 5, 1046–1054 (2018).
3. Claes, T. et al. Label-Free Biosensing With a Slot-Waveguide-Based Ring Resonator in Silicon on Insulator. *IEEE Photonics J.* 1, 197–204 (2009).
4. Palmer, R. et al. Low-Loss Silicon Strip-to-Slot Mode Converters. *IEEE Photonics J.* 5, 2200409 (2013).
5. Liu, Q. et al. Highly sensitive Mach–Zehnder interferometer biosensor based on silicon nitride slot waveguide. *Sens. Actuators B Chem.* 188, 681–688 (2013).
6. Tu, X. et al. Thermal independent Silicon-Nitride slot waveguide biosensor with high sensitivity. *Opt. Express* 20, 2640–2648 (2012).
7. Ranno, L., Sia, J. X. B., Dao, K. P. & Hu, J. Multi-material heterogeneous integration on a 3-D photonic-CMOS platform. *Opt. Mater. Express* 13, 2711–2725 (2023).
8. Khan, Z. et al. Current developments in esterification reaction: A review on process and parameters. *J. Ind. Eng. Chem.* 103, 80–101 (2021).
9. Stefan Hüfner. *Photoelectron Spectroscopy Principles and Applications*. vol. 82 (Springer-Verlag Berlin Heidelberg New York, 2003).
10. Liu, Y., Lotero, E. & Goodwin, J. G. Effect of water on sulfuric acid catalyzed esterification. *J. Mol. Catal. A Chem.* 245, 132–140 (2006).
11. da Silva, M. J., Julio, A. A. & dos Santos, K. T. Sn(ii)-catalyzed β -citronellol esterification: a Brønsted acid-free process for synthesis of fragrances at room temperature. *Catal. Sci. Technol.* 5, 1261–1266 (2015).

12. Casas, A., Ramos, M. J., Rodríguez, J. F. & Pérez, Á. Tin compounds as Lewis acid catalysts for esterification and transesterification of acid vegetable oils. *Fuel Process. Technol.* 106, 321–325 (2013).
13. Xie, W., Wang, H. & Li, H. Silica-Supported Tin Oxides as Heterogeneous Acid Catalysts for Transesterification of Soybean Oil with Methanol. *Ind. Eng. Chem. Res.* 51, 225–231 (2012).
14. Baek, H., Minakawa, M., Yamada, Y. M. A., Han, J. W. & Uozumi, Y. In-Water and Neat Batch and Continuous-Flow Direct Esterification and Transesterification by a Porous Polymeric Acid Catalyst. *Sci. Rep.* 6, 25925 (2016).